G_0-$\Delta\nu$-correlations in MRI for mapping wettability changes in porous media.

Master's Thesis

Department of Chemistry,
University of Bergen

Tord Tøllefsen

May 2022

Abstract

One of the biggest parameters deciding the dynamic behavior of fluids in the porous rock of a oil reservoir is the wettability of the mineral surface. The wettability of a surface is defined as how much a fluid will spread and be covered by one of several immiscible fluids. It is therefore paramount to understand the wettability and wetting conditions in the reservoir.

By using NMR and Magnetic Resonance Imaging (MRI) it is possible to measure some of the different dynamic properties of the molecules in a specific fluid, and how these are affected by the local environment they are trapped in. In a porous media the difference in the magnetic susceptibility ($\Delta\chi$) between the fluids and the surface will lead to spatial inhomogeneities in the static magnetic field, also known as internal gradient (G_0). G_0 scales with pore size but is also more intense closer to the surface of the media, and this can give information about the wettability of the porous media. Linewidth ($\Delta\nu$) in the MR-specter is another important parameter, that is also affected by the magnetic susceptibility and the pore sizes. By using advanced MRI-techniques for measuring the correlations between different MR-parameters and specific the correlations between G_0 and $\Delta\nu$ can be used to determine the dimension of confinement (DOC) of specific fluids.

The aim of this thesis was to measure the correlation between the internal gradient and the line width ($G_0 - \Delta\nu$), and map how the limited geometry of the fluids is affected when changing the wettability and pore geometry in a porous media based on the mineral-surface. This correlation can then describe wettability of a model system.

Acknowledgments

First and foremost, I would like to thank my supervisor John Georg Seland at the Department of Chemistry, University of Bergen. He has been very helpful during both the experimental phase with his insights and help with the technical sides of the spectrometer. He has also been paramount with his help during the analyzing and writing part.

Furthermore, I would like to thank my friends and peers for their support and motivation.

Thanks to Marthe for her support during my studies and helping me get to the finish line.

Last but not least, I would like to thank my entire family. Thanks to all my brothers and my parents for their monumental support through my studies.

Abbreviations

2D	Two dimensional
3D	Three dimensional
BW	Bandwidth
CA	Contact angle
CPMG	Carr-Purcell-Meiboom-Gill
DOC	Dimension of confinement
EOR	Enhanced oil recovery
eq	Equilibrium
FD	Free diffusion
FID	Free induction decay
FOV	Field of view
FT	Fourier transform
LOC	Localization
MR	Magnetic resonance
MRI	Magnetic resonance imaging
NMR	Nuclear magnetic resonance
RARE	Rapid acquisition with relaxation enhancement
RF	Radio frequency
SD	Standard bore
TMCS	Trimethylchlorosilane
USMB	United States bureau of mines
WB	Wide bore

Units

cm	Centimeter
Hz	Hertz
h	Hour
J	Joule
K	Kelvin
KHz	Kilohertz
m	Meter
μm	Micrometer
μs	Microsecond
ml	Millimeter
ms	Millisecond
ppm	Parts per million
rad	Radian
s	Second
T	Tesla

Symbols

θ	Angle of rotation
$\Delta\chi$	Angular frequency
P	Angular momentum
$\Delta\chi_{app}$	Apparent magnetic susceptibility difference
$T_{2,app}$	Apparent transverse relaxation time

B_1	Applied magnetic field
Z_0	Center of the slice position
Δ	Chemical shift
τ_c	Correlation time
d_1	Delay time
l_g	Dephasing length
D	Diffusion coefficient
l_D	Diffusion length
b	Diffusion term
Δ	Diffusion time
E	Echo intensity
t_E	Echo time
B_{eff}	Effective magnetic field
e	Euler's number
B_0	External magnetic field
T_2^*	Free induction decay time constant
S_i	Fluid specific saturation
V_i	Fluid specific volume
ν	Frequency
Ω_i	Frequency offset
B_{grad}	Gradient magnetic field
G	Gradient intensity
L_G	Gradient duration
γ	Gyromagnetic ratio
h	Planck's constant
$\hbar$	Plank's constant/2π
$S_{w,i}$	Immobile water saturation
k	k-space value
M_z	Longitudinal Magnetization
T_1	Longitudinal relaxation time
θ_{MA}	Magic angle
μ	Magnetic moment
Δ_χ	Magnetic susceptibility difference
G_0	Magnetic susceptibility induced internal gradient
M	Net magnetization
N_i	Number of echo points
a	Pore size
V_p	Pore volume
Φ	Porosity
^1H	Proton
L_P	Pulse length
ν_{ref}	Reference frequency
$S_{o,r}$	Residual oil saturation
x´	X-axis in the rotating frame
y´	Y-axis in the rotating frame
V_s	Sample volume
C	Scalar determined by initial spin ensemble
σ	Shielding constant
S	Signal amplitude
Δ_z	Slice thickness

Δ_f	Spectral frequency offset intervals
Δ_v	Spectral half width
I	Spin quantum number
L_s	Structural length
ρ	Surface relativity
S/V	Surface to volume ratio
t	Time
M_{xy}	Transverse magnetization
T_2	Transverse relaxation time
vd	Variable delay
V	Volume

Table of Contents

1 Introduction

One of the biggest factors in the behavior of the oil and water in the reservoir is the wettability of the porous rock. Wettability is defined as the relative preference of a surface to be covered by one of several immiscible fluids [1]. Fluid distribution in the reservoir is therefore largely dependent of the wettability of the rock surface. This makes wettability one of the most important reservoir properties to determine.

Traditionally these properties have been determined from laboratory experiments performed on core samples from the reservoir of interest. These experiments usually involve spontaneous and forced displacement of on fluid by another. The Amott-test [2] and the USBM wettability method [3] are examples of displacement experiments used for determining wettability on core samples.

Nuclear Magnetic Resonance (NMR) was discovered in 1946 by two independent research groups [4], [5]. In less than ten years NMR was being used in petrophysical laboratory investigations [6]. Since this NMR has become an integral part of petrophysical core analysis in the laboratory, as well as NMR well-logging used in oilfield exploration [7], [8].

By using NMR and Magnetic Resonance Imaging (MRI) it is possible to measure some of the different dynamic properties of the molecules in a specific fluid, and how these are affected by the local environment they are trapped in. In a porous media the difference in the magnetic susceptibility ($\Delta\chi$) between the fluids and the surface will lead to spatial inhomogeneities in the static magnetic field, also known as internal gradient (G_0). G_0 scales with pore size but is also more intense closer to the surface of the media, and this can give information about the wettability of the porous media. Linewidth ($\Delta\nu$) in the MR-specter is another important parameter, that is also affected by the magnetic susceptibility and the pore sizes. By using advanced MRI-techniques for measuring the correlations between different MR-parameters [9]–[13], and specific the correlations between G_0 and $\Delta\nu$ can be used to determine the dimension of confinement (DOC) of specific fluids.

2 Theory

2.1 Nuclear Magnetic Resonance (NMR)

Nuclear Magnetic Resonance (NMR) was discovered in 1946 [4], [5]. Since then, NMR has contributed to advancements of tremendous importance within chemistry, diagnostic medicine, and other industrial avenues. NMR is the main analytical method used in this project.

2.1.1 Fundamental NMR Theory

Nuclei containing an odd number of protons and/or neutrons will spin around their own axis causing them to possess spin angular momentum (P).

$$P = \sqrt{I(I+1)}\hbar \tag{2.1}$$

where I is the spin quantum number and $\hbar = h/2\pi$ where h is Planck´s constant ($h = 6.6256 \cdot 10^{-34}$ J s). Hydrogen, which will be used in this thesis, has a spin quantum number, I = ½. Nuclear spins are charged particles. Their precession around their own axis causes a net magnetic moment (μ). The spin angular momentum is proportional to the magnetic momentum (μ).

$$\mu = \gamma P \tag{2.2}$$

where γ is the gyromagnetic ratio of the nuclei [14]. From Equation 2.1 and 2.2 it follows that

$$\mu = \gamma\sqrt{I(I+1)}\hbar \tag{2.3}$$

This shows that a nucleus with spin quantum number I = 0 has no magnetic moment and cannot be detected using NMR spectroscopy. If a macroscopic sample containing nuclei with spin quantum number I = ½ experiences no external disturbance (no external magnetic field) the magnetic moments ($\vec{\mu}$) will orient themselves in a random direction and cancel each other, shown in Figure 1.1B [14], [15].

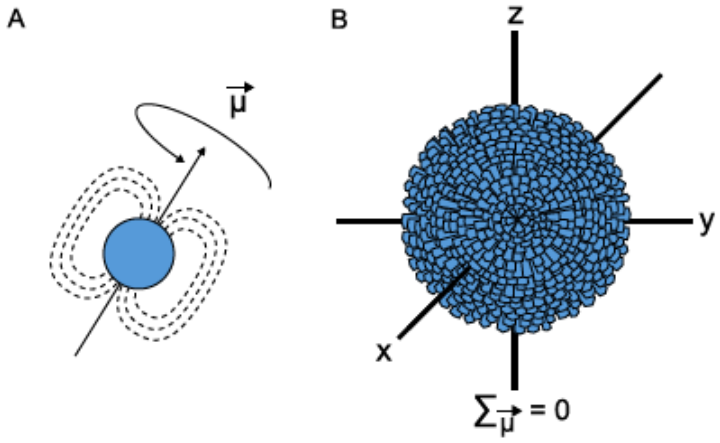

Figure 22.1: (A): Nucleus with spin angular momentum shown as a magnetic moment in the absence of an external magnetic field (B): Nuclei in a macroscopic sample randomly arranged in absence of an external magnetic field. This resulting in net magnetization is zero, due to magnetic moments cancelling each other. Figure taken from Sørgård [16].

If a nucleus with spin I = ½ and a magnetic moment $\vec{\mu}$ experiences an external magnetic field ($\overrightarrow{B_0}$), $\vec{\mu}$ will precess around $\overrightarrow{B_0}$with a frequency $\vec{\omega}$, also known as Larmor frequency (figure **2.1 A**).

If expressing the net magnetization in vector form (figure **2.2C**), the vector movement in the coordinate system, the movement can be expressed in two different ways. In a laboratory frame of reference, the magnetic moment precesses in a stationary coordinate system. This can be expressed as follows, with time dependency of $\vec{\mu}$

$$\frac{d\vec{u}}{dt} = \gamma\vec{\mu} \times \overrightarrow{B_0} \tag{2.4}$$

In the rotating frame of reference, the xy-plane is rotating with a frequency $\vec{\omega}$ which makes the magnetic moment appear as stationary [14]. If representing the rotating frame of reference in a figure, the transverse axes are marked x´ and y´. In the rotating frame of reference, the time dependance of $\vec{\mu}$ is given as

$$\frac{d\vec{u}}{dt} = \gamma\vec{\mu} \times \left(\overrightarrow{B_0} + \vec{\omega}\right) \tag{2.5}$$

This means that for the magnetic moment to appear stationary, the xy-plane must rotate with a frequency $\vec{\omega} = -\gamma\overrightarrow{B_0}$. Because when $\vec{\omega} = -\gamma\overrightarrow{B_0}$, $\frac{d\vec{u}}{dt}$ is constant and $\vec{\mu}$ is stationary.

$$\overrightarrow{\omega_L} = -\gamma\overrightarrow{B_0} \tag{2.6}$$

This frequency is called the Larmor frequency and is also the frequency at which $\vec{u}$ is rotating in the laboratory frame of reference.

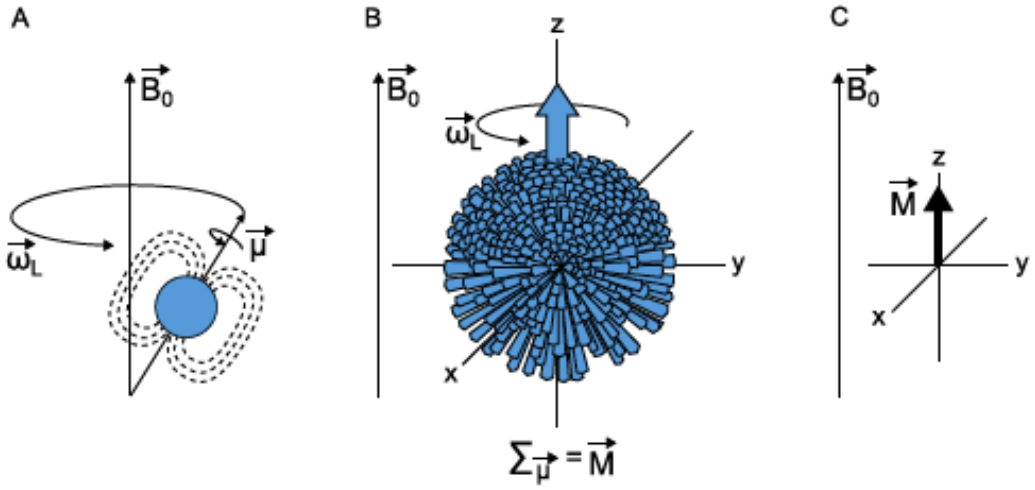

Figure 2.2 (A): Showing a nucleus with I = ½ in the presence of an external magnetic field. (B): Showing the how the sum of the precessing nuclei in a macroscopic sample in the presence of an external magnetic field ($\overrightarrow{B_0}$) creates the net magnetization vector $\vec{M}$. (C): Shows the net magnetization shown alone. Figure taken from Sørgård [16].

If an additional magnetic field is introduced to the macroscopic sample, it can be used to change the magnetization ($\vec{M}$) from z-direction, parallel to $\overrightarrow{B_0}$, to the xy-plane. This is done in NMR by using a radio frequency (RF) pulse. An RF-pulse consist of a magnetic component ($\overrightarrow{B_1}$) which changes over time, also known as oscillation. If this oscillation is equal to $\vec{\omega}$, it will interact with the net magnetization, $\vec{M}$.

In a rotating frame of reference, a resonant B_1 field will appear stationary, and the time dependence of a single moment ($\vec{\mu}$) as well as the net magnetization ($\vec{M}$) can be expressed as

$$\frac{d\vec{\mu}}{dt} = \vec{\mu}\gamma \times \overrightarrow{B_1} \tag{2.7}$$

$$\frac{d\vec{M}}{dt} = \vec{\mu}\gamma \times \overrightarrow{B_1} \tag{2.8}$$

for both equations it corresponds to the precession of the vector in question about $\overrightarrow{B_1}$ with an angular frequency $\overrightarrow{\omega_1} = -\gamma\overrightarrow{B_1}$. The angle of the vector in question from the z-axis is given by

$$\theta = \gamma B_1 L_p \tag{2.9}$$

where L_p is the duration of the RF-pulse.

2.1.2 Relaxation

Immediately after the RF-pulse is turned off, the system will start reverting to its original state, and this process is known as relaxation. The relaxation is controlled by two different relaxation mechanisms, where T_1 and T_2 are the longitudinal and transverse relaxation times. These mechanisms are described by the Bloch equations

$$\frac{dM_{x'}}{dt} = -\frac{M_{x'}}{T_2} \tag{2.10}$$

$$\frac{dM_{y'}}{dt} = -\frac{M_{y'}}{T_2} \tag{2.11}$$

$$\frac{dM_{z'}}{dt} = -\frac{M_{z'}}{T_2} \tag{2.12}$$

and equation (2.10), (2.11) and (2.12) gives

$$\frac{dM_{xy'}}{dt} = -\frac{M_{xy'}}{T_2} \tag{2.13}$$

$$\frac{dM_{z'}}{dt} = -\frac{M_0}{T_2} \tag{2.14}$$

T_1 is the longitudinal relaxation and defines how the system returns to equilibrium along the z-axis, given by the value M_0. Equation (2.15) describes how the T_1 relaxation of the magnetization increases along the z-axis.

$$M_z(t) = M_0\left(1 - A_0 e^{-\frac{t}{T_1}}\right) \tag{2.15}$$

T_2 is the transverse relaxation and describes how the magnetization goes back to equilibrium in the transverse plane. Equation (2.16) describes how the loss of phase coherence gives a loss in the magnetization in the xy-plane (M_{xy}).

$$M_{xy}(t) = M_0 e^{-\frac{t}{T_2}} \tag{2.16}$$

In a liquid sample, the loss of phase coherence in the transverse plane is caused by inter nuclei interactions and by inhomogeneities in the magnetic field (ΔB_0).

$$\frac{1}{T_2^*} = \frac{1}{T_2} + \gamma \Delta B0 \tag{2.17}$$

T_2^* is the time constant of the signal decay in the transverse plane which includes contributions from magnetic field inhomogeneities and inter nuclei interactions.

The loss of signal over time due to T_1-relaxations is not avoidable in an NMR experiment, but it is possible to avoid some of the loss of signal from T_2-relaxation. This can be done by using a spin-echo sequence. The simplest form of the sequence will be 90° - τ – 180° - τ. After the first 90° pulse, the signal will come out of focus and after a set time, τ, the signal is refocused using a 180° pulse, and this will give an echo after a time τ again. This can also be done in what's called an echo-train using a Carr-Purcell-Meiboom-Gill, CPMG, pulse sequence [17], [18]. In a CPMG pulse sequence, the signal decay caused by magnetic field inhomogeneities is refocused by 180° pulses creating an echo train. This makes the signal loss from one echo to another caused only by inter nuclei interactions.

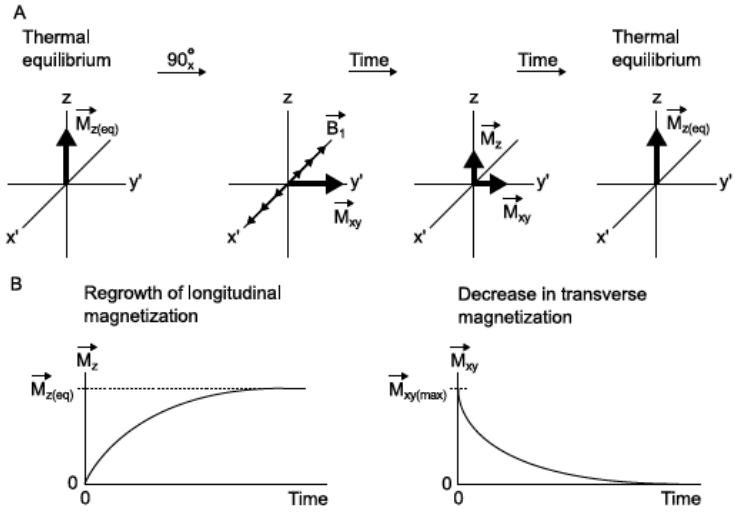

Figure 2.3 (A): Relaxation shown in a rotating frame of reference after a 90° pulse along the x-axis ($\overrightarrow{B_1}$). (B): Shows how the increase in longitudinal magnetization ($\overrightarrow{M_z}$) and the decrease in transverse magnetization ($\overrightarrow{M_{xy}}$) after $\overrightarrow{B_1}$ is switched off.

2.1.3 Relaxation in porous media

Relaxation in liquid samples, which can also be known as a bulk volume, the loss of polarization is primarily caused by inter nuclei interactions. A non-liquid-sample, such as a liquid in a porous media, will have a more complex relaxation mechanism. Liquids in porous media will also be affected by the properties of the porous matrix, quartz sand in this thesis, and the interaction between the sand and the liquid. These properties include wettability of the matrix, size of pores in the matrix, paramagnetic impurities, and magnetic susceptibility.

Excluding inhomogeneity in B_0, the relaxation can be expressed as

$$\frac{1}{T_i} = \frac{1}{T_{i,bulk}} + \rho_i \frac{S}{V} \tag{2.18}$$

Where i = 1,2, ρ_i is the surface relativity term, and $\frac{S}{V}$ is the surface to volume ratio of the pores.

Usually, $\rho_i \frac{S}{V} \gg \frac{1}{T_{i,bulk}}$, which leads to

$$\frac{1}{T_i} \approx \rho_i \frac{S}{V} \tag{2.19}$$

If a porous media is placed in a strong uniform magnetic field (B_0), this magnetic field will induce a spatially inhomogeneous magnetic field in the sample. This inhomogeneous magnetic field is dependent on the pore structure of the porous media and the difference in magnetic susceptibility ($\Delta\chi$). This magnetic susceptibility is a product of the difference in magnetism of different phases present in the sample. When a liquid filled porous media is placed in a strong uniform magnetic field, the apparent difference in magnetic susceptibility ($\Delta\chi_{app}$) between the liquid and the solid matrix includes internal magnetic field gradients (G_0) which distorts the magnetic field [16].

$$G_0 \approx \frac{B_o \Delta\chi_{app}}{a} \tag{2.20}$$

Equation (2.20) shows that the internal magnetic field gradient (G_0) is proportional to the uniform magnetic field (B_0) and the apparent magnetic susceptibility ($\Delta\chi_{app}$), and inversely proportional with the pore size (a). This shows that the internal gradients will be biggest in the smallest pores of the sample.

The magnetic moment of the molecules in the liquid will collide with the walls of the pore in a porous media and energy will be released. This will give an extra attribution to T_1- and T_2-relaxation.

Using a form of CPMG pulse sequence during the acquisition of a non-liquid-sample it's the apparent transverse time $T_{2,app}$, that is recorded.

This can be expressed as

$$\frac{1}{T_{2,app}} = \frac{1}{T_2} + \rho_2 \frac{S}{V} + b \tag{2.21}$$

Where ρ_2 is the surface relativity term for transverse relaxation, $\frac{S}{V}$ is the surface to volume ratio of the pores and b is the diffusion term[19]. This diffusion term is introduced as a result of the

internal magnetic fields, caused by the difference in magnetic susceptibility between the matrix and fluids in the pore space. As a result of the internal magnetic field gradients, caused by the difference in magnetic susceptibility between the fluids in the pores and pore matrix, a diffusion term is introduced. The M_{xy} magnetization in a porous sample as a function of time is given as

$$\frac{M_{xy}(t)}{M_{xy}(0)} = e^{-\left(\frac{1}{T_{2,app}}+\rho_2\frac{S}{V}+b\right)} \tag{2.22}$$

The longitudinal relaxation (T_1) is not affected by the diffusion or γB_0, but it is affected by the surface relaxivity associated with porous samples. The recovery of $\overrightarrow{M_z}$ in a porous sample can be expressed as

$$\frac{M_z(t)}{M_z(eq)} = 1 - C\left(e^{-\left(\frac{1}{T_1}+t\rho_1\frac{S}{V}\right)}\right) \tag{2.23}$$

Where ρ_1 is the relaxivity term associated with longitudinal relaxation.

2.1.4 Free Induction Decay (FID) and Fourier transformation (FT)

After an excitation pulse, the signal needs to be recorded. After the excitation pulse, the net magnetization is precessing in the xy-plane, and this induces a current in the spectrometer's receiver coil. This recording of the x- and y-component of $\overrightarrow{M_{xy}}$ as a function of time is what's known as Free Induction Decay (FID). The FID measures the NMR signal as a time-domain, but to interpret the signal it needs to be presented as a function of frequency. This is achieved by Fourier transform (FT) [14], [20].

2.2 Magnetic Resonance Imaging (MRI)

In Magnetic Resonance Imaging (MRI), the Larmor frequency is made spatially dependent by adding additional magnetic field gradients, B_{grad}, that vary the samples experienced magnetic field. This can be done in all directions in the sample [21], [22]. This is in contrast with conventional NMR spectroscopy where the aim is to achieve a high level of homogeneity of the magnetic field through the entire sample.

$$B_{grad} = B_0 + G * r \tag{2.24}$$

Where $G = \left(\frac{\partial B_z}{\partial x}, \frac{\partial B_z}{\partial y}, \frac{\partial B_z}{\partial z}\right)$ is the position independent magnetic field gradient and $r = (x, y, z)$ is the position. The gradients, also known as gradient pulses, are added in short periods during a scan. Gradients can only be active in one direction at the time, but it is possible to have gradients in all directions (x,y,z). These gradients are used in different measures during the acquisition with three distinct tasks: slice selection, frequency-encoding, and phase-encoding. When gradients are presents the Larmor equation (Equation 2.6) can be expressed as

$$\omega(r) = \gamma(B_0 + G) * r \tag{2.25}$$

Slice selection in MRI is determining the thickness of the image wanted, or slice thickness. Slice selection is usually achieved by applying a magnetic field gradient along the z-axis (G_z) and creating a spatially dependent Larmor frequency along the z-axis. This gradient (G_z) is kept active during the excitation pulse. To change the thickness of the slice it is possible to alter the strength of G_z while keeping the bandwidth the same or change the bandwidth with the same G_z.

$$\Delta z = \frac{\Delta\omega}{|\gamma G_z|} \tag{2.26}$$

Equation 2.23 shows the relationship between slice thickness (Δz), pulse bandwidth ($\Delta\omega$) and the strength of the gradient (G_z). In multi-slice selection sequences, the same G_z is used but the RF-pulse for each excitation is altered. Each RF pulse has the same bandwidth but different frequency and will therefore change the slice selection for the excitation in the sample.

After the G_z and the excitation pulse have excited the nuclei in the slice another gradient is applied in the y-direction. This is called phase encoding (G_y) and is used to cause a phase shift before the signal is recorded. It ensures a spatial encoding along the y-axis. For an image with 10_y by 1000_x resolution there needs to be done using ten phase encoding steps. While keeping all other parameters the same the sequence needs to be done with ten different G_y values.

After the phase encoding, the signal is recorded while a gradient along the x-axis is turned on (G_x). This process is known as frequency encoding, and this gives the position of the signal along the x-axis. The signal will be recorded close to a readout-gradient (G_{RO}) which produces one of the two visual axes of the image. Magnetization of G_{RO} and the frequency measured is determined by two parameters, Field of View (FOV) in the direction of the frequency encoding and the Nyquist frequency (ω_{NQ}).

$$\Delta\omega_{RO} = 2\omega_{NQ} = \gamma\Delta(G_{RO} * FOV_{RO}) \tag{2.27}$$

$\Delta\omega_{RO}$ is the total range of frequency in the image, G_{ro} is chosen so that protons in the end of the FOV_{RO} precesses at the Nyquist frequency of the image. FOV_{RO} becomes smaller with an increase of G_{RO}, and constant ω_{NQ} and ω_{RO}.

2.2.1 Internal Magnetic Field Gradients

When analyzing liquid samples in high field NMR spectroscopy, great efforts are made to ensure that the magnetic field is homogeneous throughout the entire sample volume. The difference of the magnetic field (ΔB_0) is proportional to the spectral half width ($\Delta\nu$), and inversely proportional to the time constant (T_2^*) of the FID. An increase in field inhomogeneities will therefore result in a broadening of linewidth and shorten the lifespan of the observed signal. [8]

$$\Delta\nu = \frac{1}{\pi T_2^*} \approx \frac{1}{T_2} + \gamma\Delta B_0 \tag{2.28}$$

Liquid samples in superconducting magnets give an almost homogeneous magnetic field through the entire sample ($\Delta B_0 \approx 0$). For liquids in a porous media, the magnetic field will not be homogenous. This is because the apparent difference in magnetic susceptibility ($\Delta\chi_{app}$) between the liquid and the solid matrix induces internal magnetic field gradients (G_0), this distorts the magnetic field [16].

Internal gradients can be measured by implementing a modified 2D CPMG sequence where the number 180° pulses in the echo train is varied over a constant time period [23]. This difference in the number of pulses varies the echo time as well. The echo time is defined as

$$t_E = 2\tau' + L_{P(180)} \tag{2.29}$$

Where τ' is the spacing on each side of the 180° pulse and $L_{P(180)}$ is the length of the 180° pulse. Both the external magnetic field and the geometry of the porous media affect the strength of the internal magnetic field gradients (G_0) [24]–[27].

$$G_0 \approx \frac{B_0 \Delta\chi_{\text{app}}}{a} \tag{2.30}$$

Self-diffusion caused by kinetic energy is the random Brownian motion of molecules. In a porous media, this is hindered by the pore matrix.

Three length scales are used when discussing the diffusion term for a CPMG experiment with n echoes and a constant G_0 [25].

$$\frac{M(t_E)}{M(t_E = 0)}\ e^{-t_E \rho_2 \frac{S}{V} - \frac{1}{12} D\gamma^2 G_0^2 t_E^3} \tag{2.31}$$

The diffusion length, $l_D = (Dt_E)^{\frac{1}{3}}$, is the length a molecule travels due to diffusion during the echo time t_E. The dephasing length, $l_g = \left(\frac{2\pi D}{\gamma G_0}\right)^{\frac{1}{3}}$, is the distance the molecules must move to dephase 2π radians. The structural length, $l_s = a$, which in porous media is defined as the pore diameter [24], [25]. Using these length scales gives three diffusion regimes known as the Motional Averaging (MAV) regime, the Localization (LOC) regime and the Free Diffusion (FD) regime.

MAV regime applies when $l_s \ll l_D$ and $l_s \ll l_g$, valid for samples with small pore sizes and a low $B_0 \Delta\chi_{app}$ term. LOC regime applies when $l_g \ll l_D$ and $l_g \ll l_s$, valid for samples with a very short dephasing length (l_g) and a large $B_0 \Delta\chi_{app}$ term. FD regime applies when $l_d \ll l_s$ and $l_D \ll l_g$, valid for samples with large pores. The internal gradient values in FD regime are moderate during the echo time t_E.

In this thesis, a 11.7T NMR spectrometer was used which is associated with a high $B_0\Delta\chi_{app}$ term, and therefore the molecules are most likely subjected to a regime between the LOC and FD regime.

Sørgård et al.[10] expressed how correlations between Δν and G_0 can be used to convert the G_0 distribution to a fluid specific dimension of confinement (DOC) distribution. DOC is fluid specific and gives a fluid specific "pore size" expressed as

$$DOC = \frac{2\pi\Delta\nu}{\gamma G_0} \tag{2.32}$$

In this thesis, water and oil , two immiscible fluids, were used, and since DOC is fluid specific it is not the pore size found, but rather a measure of the fluid confinement [10], [16].

2.3 Petrophysical properties

2.3.1 Porosity and permeability

Porosity (ϕ) is a measurement of a porous medium's fluid storage capacity.[1] The porosity is defined as

$$\phi = \frac{V_p}{V_s} \tag{2.33}$$

Where V_p is the pore volume and V_s is the sample volume. Porosity is split in two parts, effective porosity (ϕ_{eff}) which are connected pores and will let a fluid through the porous medium. The residual porosity (ϕ_{res}) is closed pores with no connections.

Permeability is directly dependent on the effective porosity of a porous media. Permeability is a measurement of a porous medium´s ability to allow fluids to pass through it. The absolute permeability through the entire pore system is constant but can only be found if there is just one fluid present. If there are two or more immiscible fluids in the system, they will affect the permeability of each other, and the effective porosity is measured.

Absolute permeability (k) was defined by Henry Darcy in 1856, and Darcy´s law is given with a linear, horizontal flow for a non-compressible fluid

$$Q = \frac{k * A}{\mu} * \frac{\Delta p}{L} \tag{2.34}$$

where Q is the flow rate, A is the cross-sectional area of the cylinder, μ is the viscosity, Δp is the difference in pressure though the sample and L is the length of the cylinder. For formula (2.X) to work, the sample needs to be totally saturated by only one fluid and the viscosity must be constant [1].

2.3.2 Saturation

In one pore space, multiple immiscible fluids may be present at one time. The fluid specific saturation (S_i) is defined as

$$S_i = \frac{V_i}{V_p} \tag{2.35}$$

where V_i is the volume of a specific fluid and V_p is the pore volume [1].

2.3.3 Wettability

The wettability of a surface is defined as how much a fluid will spread and be covered by one of several immiscible fluids. In this project, oil and water are the two immiscible fluids used. In oil recovery, it is paramount to understand the wettability and wetting conditions in the reservoir.

On flat surfaces, the wettability is determined with contact angle measurements, where the angle created between the drop of the densest phase and the surface determines the wettability of the surface. A contact angle below 90° give water-wet and above 90° gives oil-wet. Surfaces with contact angles around 90° can be considered neutral-wet [1].

2.3.4 Wettability alteration

Chemically induced wettability alteration can be used for turning a water-wet surface oil-wet. In this thesis, quartz sand is used, originally water-wet, and made oil-wet through exposing the sand to a solution of trimethylchlorosilane in heptane. In this process, the trimetylsilane-groups adsorbs to the OH on the quartz surface, and this turns the quartz from water-wet, hydrophilic, to oil-wet, hydrophobic [16].

3 Materials and methods

3.1 Materials and hardware

Table 3.1: Solids used in this thesis

Solids	**Provider**	**Particle size range**
NC4X quartz	The Quartz Corp	50-260 μm

Table 3.2: Liquids used in this thesis

Liquids	**Provider**	**Specifics**
Light mineral oil	Sigma Aldrich	
Heptane	Sigma Aldrich	
Trimethylchlorosilane	Sigma Aldrich	5% TMCS in heptane
Distilled water	University of Bergen	

3.2 Sample preparation

A model core sample had been manufactured to allow for displacement experiments in pure quartz sand, and this was used in this thesis. All components of the cell are made of plexi-glass which are non-magnetic, and this allows for displacement experiments to be performed inside the NMR spectrometer. The sample consists of quartz sand being mechanically held in place inside of the plexi-glass cell. Filters were equipped in the cell to prevent sand from escaping into the inlet and outlet tubing. The cell was saturated with distilled water by vacuum before every experiment.

In this thesis, five different samples of quartz sand were used in the cell. One consisted of 100% untreated quartz sand (water-wet), one consisted of 100% treated quartz sand (oil-wet), one with a 50% water-wet and 50% oil-wet mixture by weight, one with a 70% water-wet and 30% oil-wet mixture by weight and the last with a 30% water-wet and 30% oil-wet mixture by weight. The three blended mixtures were mixed by hand for 60 seconds each.

The quartz sand was treated to become oil-wet through a salinization process. Pure quartz sand was submerged in trimethylchlorosilane (TCMS) 5% in heptane solution for 20 minutes at room temperature. This mixture was shaken every 2 minutes. After this, the sand was cleaned 5 times in heptane and dried in a fume hood. In this process, trimethylsilane adsorbs to the OH-sites of the quartz surface and making it hydrophobic.

3.3 Displacement experiments

The samples were saturated with distilled water before each displacement experiment. The cell has a known volume, and the porosity of the sample was determined by weighing the cell before and after the cell was saturated with water. Imbibition is the process of absorbing a wetting face into a porous matrix, and drainage is the process of forcing a nonwetting phase into a porous media. In this thesis, the imbibition and drainage flow during the displacement experiments was controlled using a Nexus 5000 syringe pump with a flow rate of 30 mL/hour. This pump was connected to the cell while the cell was situated inside the bore of a Bruker 500 MHz WB spectrometer.

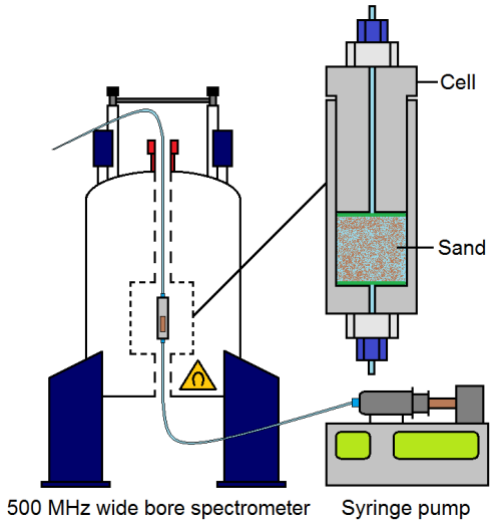

Figure 3.1 Overview of how the liquid was pumped through the flow cell while the cell was placed inside the spectrometer. Figure taken from Sørgård [16].

3.4 Instruments: NMR/MRI and pump

In this thesis, a wide bore (WB) Bruker Ascend 500 MHz spectrometer was used. The MRI probe used was a commercial MicWB40 micro imaging probe, and it was used with the Bruker Micro 2.5 gradient system, which is capable of delivering gradient strengths of up to 1.5 Tm^{-1}.

The pump used for the displacement experiments was a Nexus 5000 syringe pump. The pump's flow rate control has an accuracy of ±0.35% of the set rate and reproducibility within 0.05%.

3.5 Methods

3.5.1 Spin echo and CPMG

A spin echo sequence consists of a minimum of two radiofrequency (RF) pulses, one 90°-pulse and one or more 180°-refocusing pulses. In spin echo, the signal loss associated with inhomogeneities in the external magnetic field is refocused with the 180° pulses resulting in an echo.[14]

After the 90° pulse is switched off the transverse vectors, which at start are in phase, will precess at different speeds due to the variation in the magnetic field (B_0). Vectors with a high Larmor frequency will rotate faster than those with lower Larmor frequencies. After a time (τ) a 180° refocusing pulse is sent and this will flip the vectors 180° in the x,y-plane. The vectors with the highest speeds will catch up with the vectors with the lower speeds, and result in the vectors being in phase again after a time (τ). Figure 3.2C shows a vector diagram of the Carr-Purcell-Meiboom-Gull (CPMG) pulse sequence [17], [18], which is based on the spin echo and uses a series of 180° pulses to refocus the signal several times. This gives a series of echoes where the signal attenuation between echoes is caused only by inter-nuclear relaxation. The time constant of the echo attenuation is T_2^{-1}.

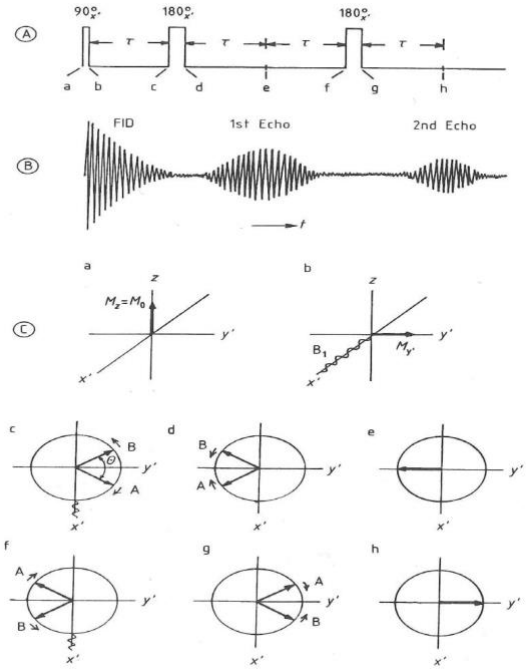

Figure 3.2 Carr-Purcell spin echo experiment. A: Diagram of the pulse sequence ($90°_{x'} - \tau - 180°_{x'} - \tau - (\text{echo } 1) - \tau - 180°_{x'} - \tau - (\text{echo } 2) \ldots \text{etc.}$). B: Time domain spectrum (FID followed by two echos). C: Vector diagram of the pulse sequence shown in A. Figure taken from Friebolin [14].

3.5.2 Modified CPMG

In this thesis, a modified CPMG sequence [16], [23] was used. In the modified CPMG sequence DG_0^2 encoded signal decay is a result of varying the time available for irreversible dephasing due to diffusion of the internal gradient. This sequence was used because of the internal gradients (G_0) induced by the magnetic susceptibility differences between the fluids and the solid matrix in the porous media. In a modified CPMG sequence the time from excitation to the signal is recorded is constant through the entire sequence. This is different from the normal CPMG which produces an echo train where the signal decay between echoes is T_2^{-1}weighted. As the signal in a normal CPMG is refocused from one echo to another the intensity of an echo is a function of time elapsed since excitation. In a modified CPMG conversely the time (τ) between the 180° refocusing pulses is varied by varying the number (n) of 180°refocusing pulses over the constant time (T). This is shown in figure **3.3.**

This thesis used the same parameter as Sørgård[10], [12], [16] with *n* 180° pulses varying from 32 to 1 in 32 steps. The constant time (T) was set to T=50ms, so that the signal is close to zero when only one 180° pulse is applied. Pulse lengths of the hard 90° and 180° were 44 and 88 μs. The gradient strength during slice selection (G_z) was $1.4797 * 10^{-4}\mathrm{T}^{-1}\mathrm{m}^{-1}$ and the bandwidth was 6300 Hz.

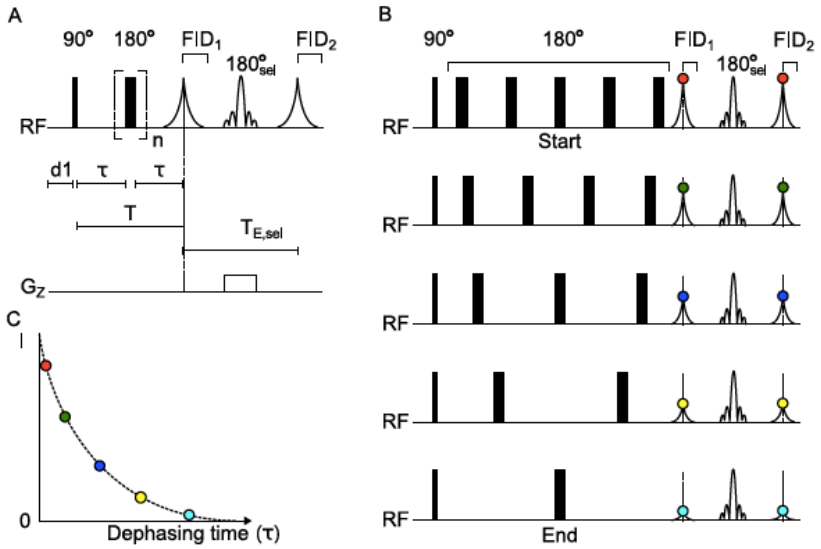

Figure 3.3 The modified CPMG from Sørgård[16] used in this thesis. A: If FID_1 is recorded the sequence is non-spatially resolved and spatially resolved if FID_2 is recorded. B: Showing how, with 5 steps, the sequence changes when n 180° pulses are varied from five to one. C: Showing how the resulting decrease in signal intensity (I) as a function of the dephasing time (τ). Figure from Sørgård [16].

3.5.3 Spin echo in MRI

All MR-images presented in this thesis were recorded using a Rapid Acquisition with Relaxation Enhancement (RARE) sequence. The parameters for these acquisitions were set equal to that in Sørgård [10], [16]. The RARE factor was set to 1 to maximize the signal in the fluid saturated porous samples. A RARE factor of 1 uses only one refocusing pulse and will therefore be equal to a regular spin echo. The echo time was set to 2.91 ms and repetition time was set to 1 s to ensure T_1 weighting in images were water and oil was present at the same time.

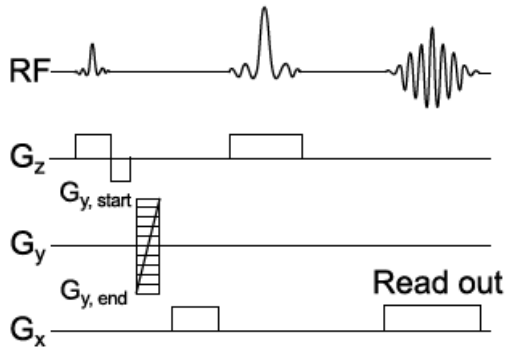

Figure 3.4 MRI spin echo pulse sequence with axial slice selection (G_Z), phase encoding in the y-direction (G_Y) and frequency encoding in the x-direction (G_X). Figure from Sørgård[16].

3.5.4 Data processing

All data from the acquisitions was first processed in TopSpin, and MR-images in ParaVision. The data was then further processed in MATLAB. The scripts used in MATLAB can be seen in appendix **A**, and the correlation data was analyzed using a 2D-ILT software [28].

4 Results

4.1 Displacement experiments

4.1.1 Water-wet sample, WW.

Primary water drive

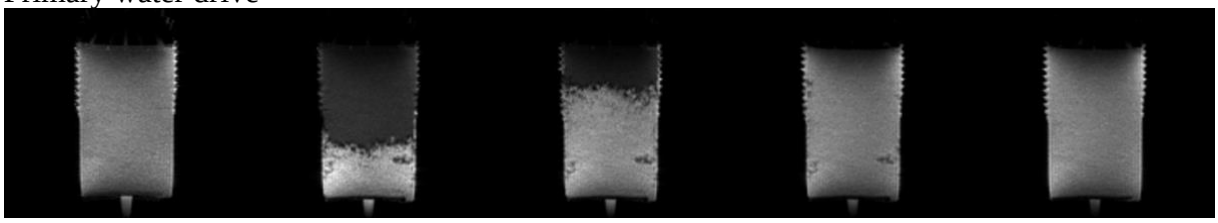

S_w=1 0.3PV 0.5PV 1PV 5PV ($S_{w,i}$)

Primary oil drive

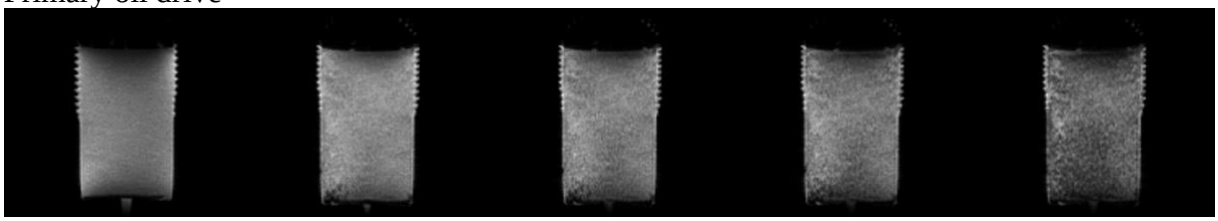

$S_{w,i}$ 0.3PV 0.5PV 1PV 5PV ($S_{o,r}$)

Figure 4.1 Primary oil drive and primary water drive for the water-wet sample. MR-images used to visualize the displacement fronts during the process. $S_w = 1$ is where the sample is 100% saturated with water, and $S_{w,i}$ is the irreducible water saturation after 5PV oil through the sample. $S_{o,r}$ is the residual oil saturation after the injection of 5PV water.

The displacement front is visualized in the MR-images. For the primary oil drive a distinctive front is seen throughout the experiment. For the primary water drive this is not as visible, but there is a clear distinction between $S_{w,i}$ and 5PV water injected.

4.1.2 Oil-wet sample, OW.

Primary oil drive - imbibition

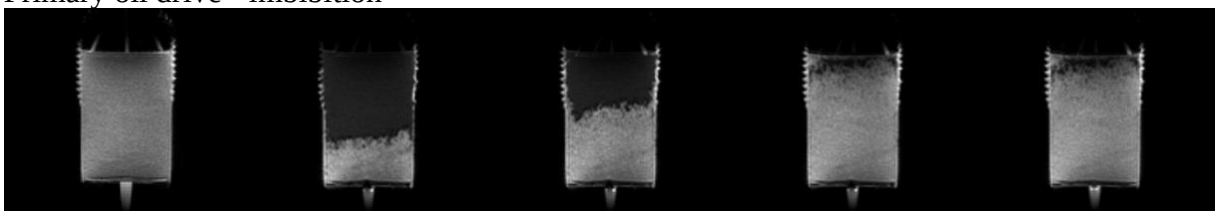

S_w=1 0.3PV 0.5PV 1PV 5PV ($S_{w,i}$)

Primary water drive

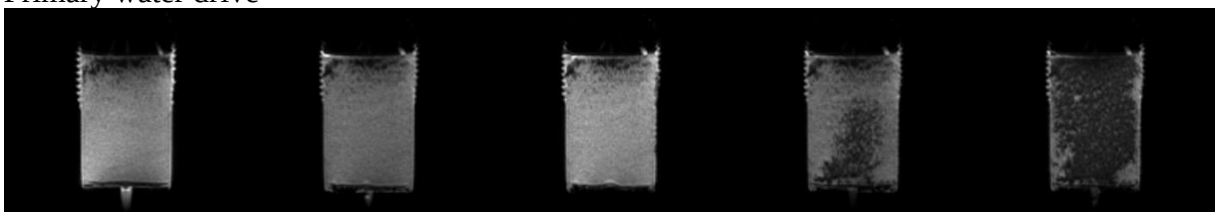

$S_{w,i}$ 0.3PV 0.5PV 1PV 5PV ($S_{o,r}$)

Figure 4.2 Primary oil drive and primary water drive for the oil-wet sample. MR-images used to visualize the displacement fronts during the process. $S_w = 1$ is where the sample is 100% saturated with water, and $S_{w,i}$ is the irreducible water saturation after 5PV oil through the sample. $S_{o,r}$ is the residual oil saturation after the injection of 5PV water.

For the oil-wet sample the displacement front is also very uniform during the primary oil drive. As for the water-wet sample the front is not as visible for the primary water drive, but also here there is a clear distinction between the MR-image of $S_{w,i}$ and 5PV water injected

4.1.3 Sample containing 50% water-wet and 50% oil-wet sand, 50/50 WW/OW.

Primary oil drive

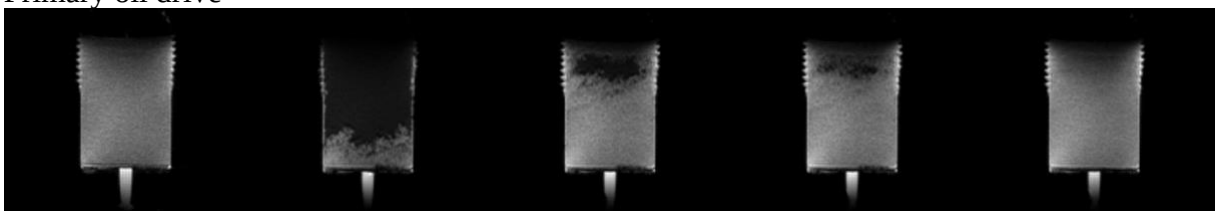

S_w=1 0.3PV 0.5PV 1PV 5PV ($S_{w,i}$)

Primary water drive

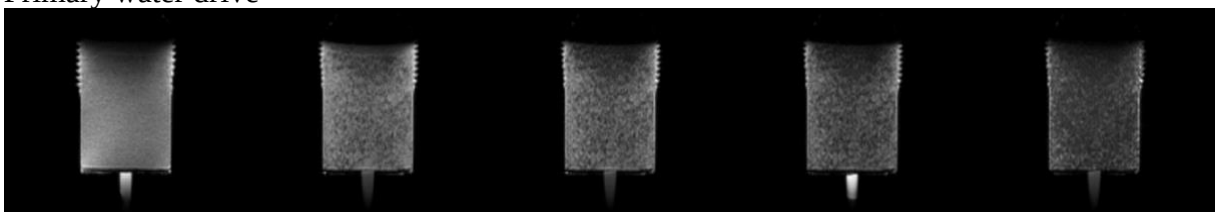

$S_{w,i}$ 0.3PV 0.5PV 1PV 5PV ($S_{o,r}$)

Figure 4.3 Primary oil drive and primary water drive for a sample containing 50% water-wet and 50% oil-wet sand. MR-images used to visualize the displacement fronts during the process. S_w = 1 is where the sample is 100% saturated with water, and $S_{w,i}$ is the irreducible water saturation after 5PV oil through the sample. $S_{o,r}$ is the residual oil saturation after the injection of 5PV water.

The sample containing a mixture of 50% water-wet and 50% oil-wet sand the displacement front of the primary oil drive is not as uniform as for the water-wet and oil-wet samples. The MR-images show viscous fingering[29], [30] during the primary oil drive. As for the previous samples this also shows no uniform front during the primary water drive, but clearly shows a distinctive difference between $S_{w,i}$ and 5PV water injected.

4.1.4 Sample containing 70% water-wet and 30% oil-wet sand, 70/30 WW/OW.

Primary oil drive

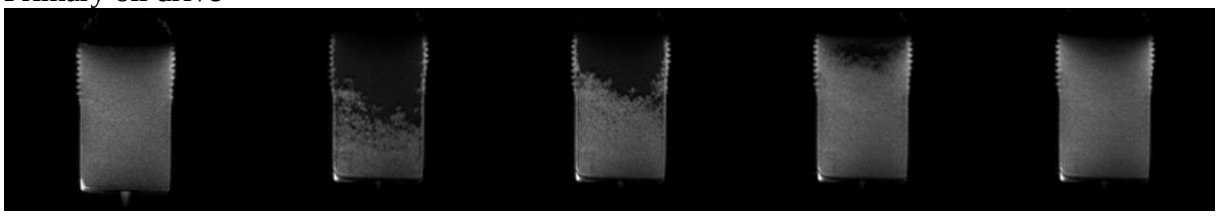

S_w=1 0.3PV 0.5PV 1PV 5PV ($S_{w,i}$)

Primary water drive

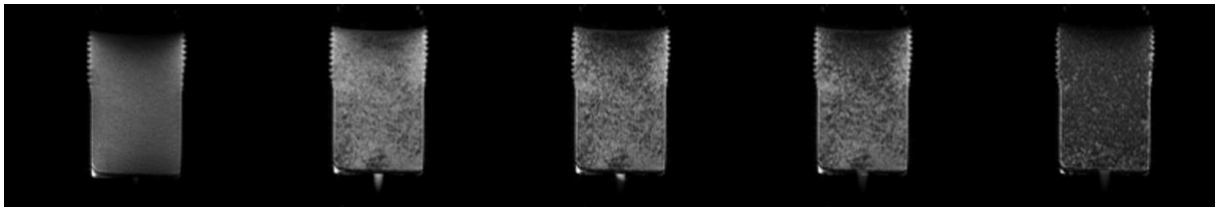

$S_{w,i}$ 0.3PV 0.5PV 1PV 5PV ($S_{o,r}$)

Figure 4.4 Primary oil drive and primary water drive for a sample containing 70% water-wet and 30% oil-wet sand. MR-images used to visualize the displacement fronts during the process. S_w = 1 is where the sample is 100% saturated with water, and $S_{w,i}$ is the irreducible water saturation after 5PV oil through the sample. $S_{o,r}$ is the residual oil saturation after the injection of 5PV water.

This sample does also not show a uniform displacement front during the primary oil drive, and viscous fingering can be seen in this sample also. As for all the previous samples this also shows no uniform front during the primary water drive, but clearly shows a distinctive difference between $S_{w,i}$ and 5PV water injected.

4.1.5 Sample containing 30% water-wet and 70% oil-wet sand, 30/70 WW/OW.

Primary oil drive

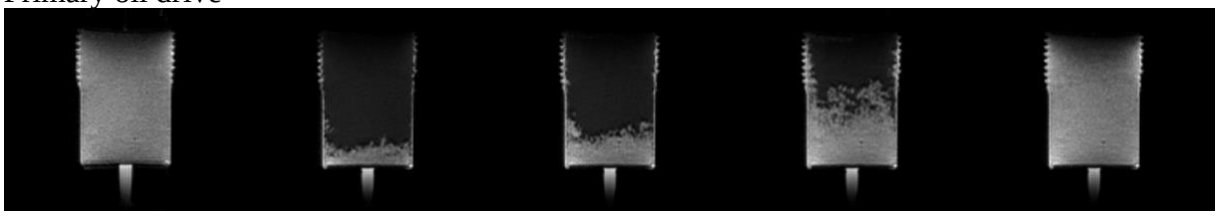

S_w=1 0.3PV 0.5PV 1PV 5PV ($S_{w,i}$)

Primary water drive

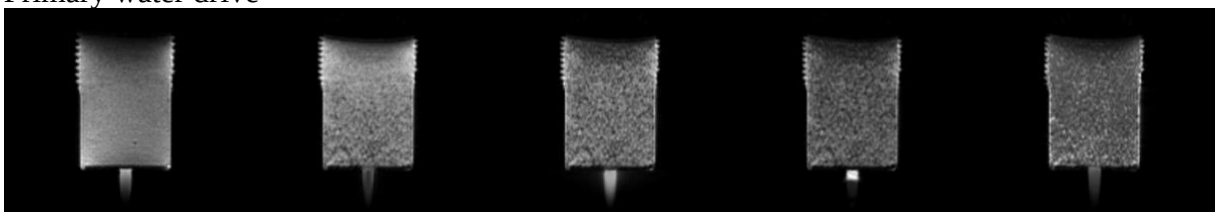

$S_{w,i}$ 0.3PV 0.5PV 1PV 5PV ($S_{o,r}$)

Figure 4.5 Primary oil drive and primary water drive for a sample containing 30% water-wet and 70% oil-wet sand. MR-images used to visualize the displacement fronts during the process. S_w = 1 is where the sample is 100% saturated with water, and $S_{w,i}$ is the irreducible water saturation after 5PV oil through the sample. $S_{o,r}$ is the residual oil saturation after the injection of 5PV water.

This sample shows a different behavior than what is expected. From 0.3PV to 1PV of the primary oil drive it can be thought that not the right volume of oil has been injected into the sample. This outlier is seen in both measurements which somewhat exclude a user error, but it is also possible that the pore volume for both these samples are miscalculated. For further use in this thesis the 1PV of the 30% water-wet and 70% oil-wet sample is used as this is what is seems to be closer to 0.5PV of the other samples.

4.2 Comparison of repeated measurements for fluid specific DOC distributions

All samples, with repeated measurements, were recorded in every step of the displacement experiment in five different 1 mm axial slices. These slices were at -6 mm, -2 mm, iso-center, +2 mm and +6 mm.

For comparison of the repeated measurement, the water signal at -6 mm and +6 mm slices at 0.5PV of the primary oil drive and the primary water drive were used. Presented here is the

water signal of +6mm slices of the 0.5PV primary oil drive. All other specters can be seen in appendix **B**.

4.2.1 Water signal for the fluid specific DOC distributions

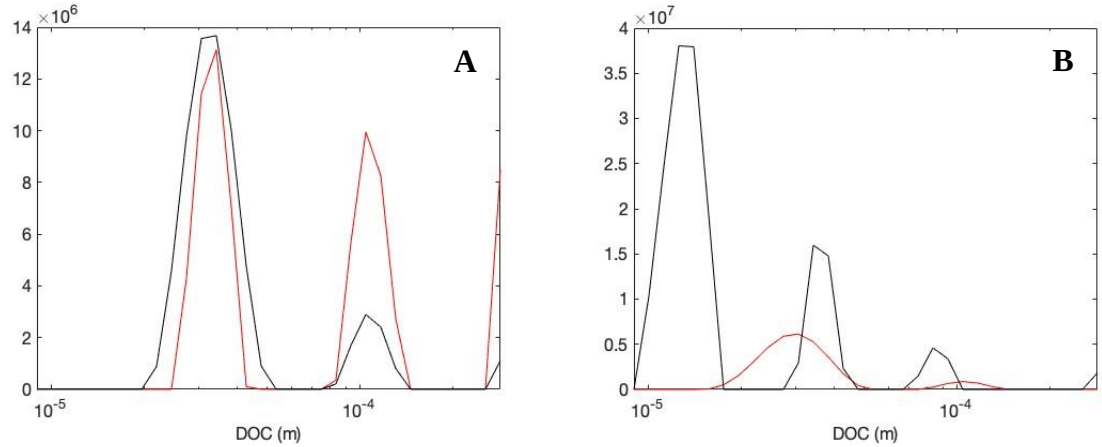

Figure 4.6 DOC distributions in the primary oil drive (0.5PV) at +6mm slice for water-wet (A) and oil wet (B) sample.

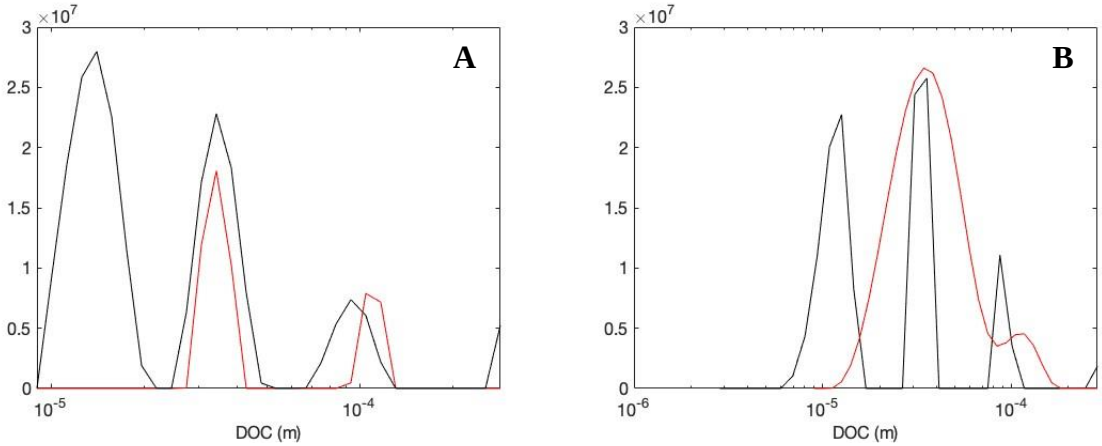

Figure 4.7 DOC distributions in the primary oil drive (0.5PV) at +6mm slice for 50% water-wet and 50% oil-wet sand (A) and 70% water-wet and 30% oil-wet sand (B) sample.

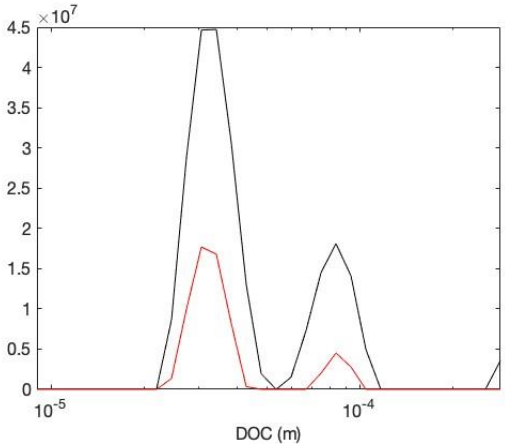

Figure 4.8 DOC distributions in the primary oil drive (0.5PV) at +6mm slice for 30% water-wet and 70% oil-wet sand.

Figure **4.6-4.8** shows both the repeated measurements of the distributions of DOC for the water signal at 0.5PV primary oil drive in all samples. Some of the measurements show a distinctive difference in intensity between the measurements, but it is seen that generally the distribution of DOC is at the same sizes, in the 10^{-5} to 10^{-4} m range.

4.2.2 Oil signal for the fluid specific DOC distributions

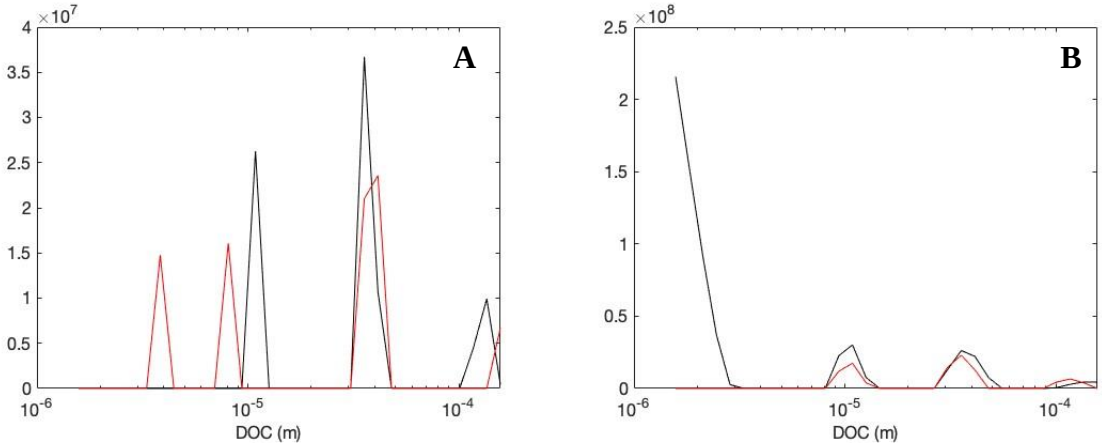

Figure 4.9 DOC distributions in the primary oil drive (0.5PV) at +6mm slice for water-wet (A) and oil wet (B) sample.

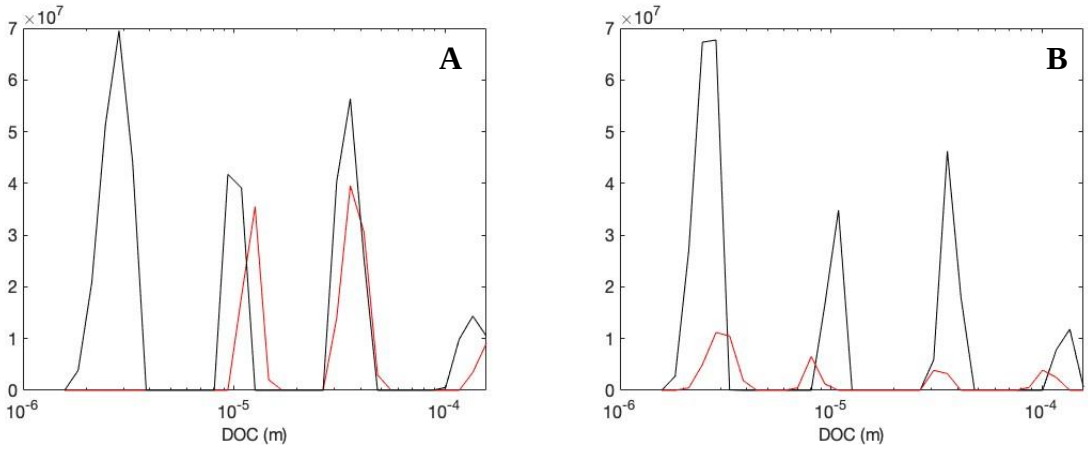

Figure 4.10 DOC distributions in the primary oil drive (0.5PV) at +6mm slice for 50% water-wet and 50% oil-wet sand (A) and 70% water-wet and 30% oil-wet sand (B) sample.

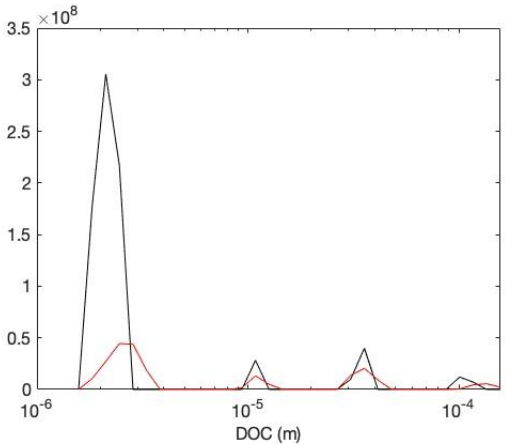

Figure 4.11 DOC distributions in the primary oil drive (0.5PV) at +6mm slice for 30% water-wet and 70% oil-wet sand.

As for the water signal of the DOC, the oil signal shows some of the same tendency. Some of the measurements show a distinctive difference in intensity between the measurements, but it is seen that generally the distribution of DOC is at the same sizes, in the 10^{-6} to 10^{-4} m range.

4.3 The dimension of confinement

4.3.1 Water signal for the fluid specific DOC distributions

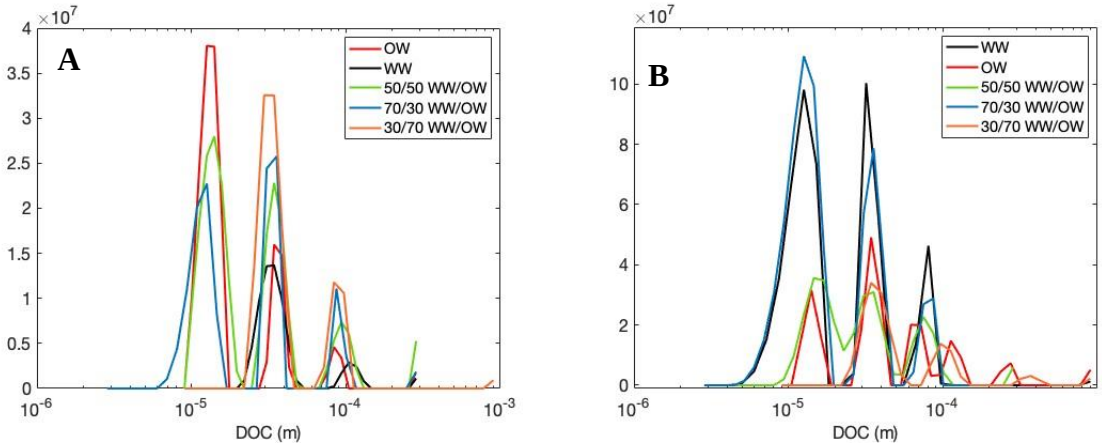

Figure 4.12 DOC distributions at +6mm for primary oil drive (A) and primary water drive (B).

Figure **4.12** shows the DOC distributions for both the primary oil drive and the primary water drive, at +6mm. In **4.12A** it is possible to see that during the primary oil drive the samples with oil-wet sand present (except for 30/70 water-wet/oil-wet, outlier) there is a peak in lower part of the DOC distribution. The water-wet sample does not have this peak.

For the primary water drive (figure **4.12B**) it is shows that the two samples with the highest amount of water-wet sand (WW and 70/30 WW/OW) in the sample have peaks at the lowest DOC distributions again. This peak appears to be in the same region as the lowest for the primary oil drive.

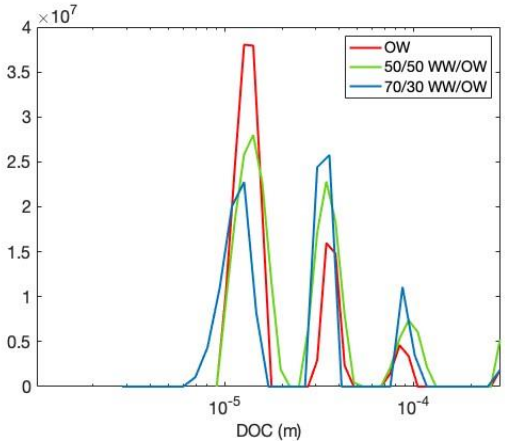

Figure 4.13 DOC distributions at +6mm for primary oil drive (0.5PV) for oil-wet (OW), 50/50 water-wet (WW)/oil-wet (OW) and 70/30 WW/OW sample.

Figure **4.13** is using the same data as figure **4.12A** without the DOC distributions from the water-wet and 30/70 water-wet/oil-wet samples. This is done to remove the water-wet sample without the peak in the lowest region of DOC distributions and remove 30/70 water-wet/oil-wet sample which proved to be an outlier.

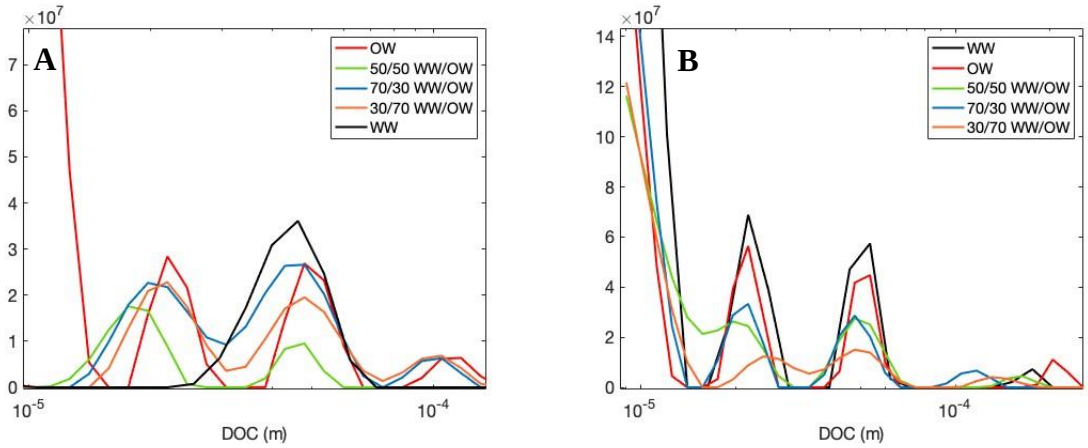

Figure 4.14 DOC distributions at -6mm for primary oil drive (A) and primary water drive (B).

This figure shows the DOC distributions at -6mm axial slice for both the primary oil and water drive. In the primary oil drive (figure **4.14A**) it is shown that the water-wet sample has no peak in the lowest DOC distribution area, as the samples with oil-wet sand. For the primary water drive (figure **4.14B**) the peaks in the DOC distributions are very similar.

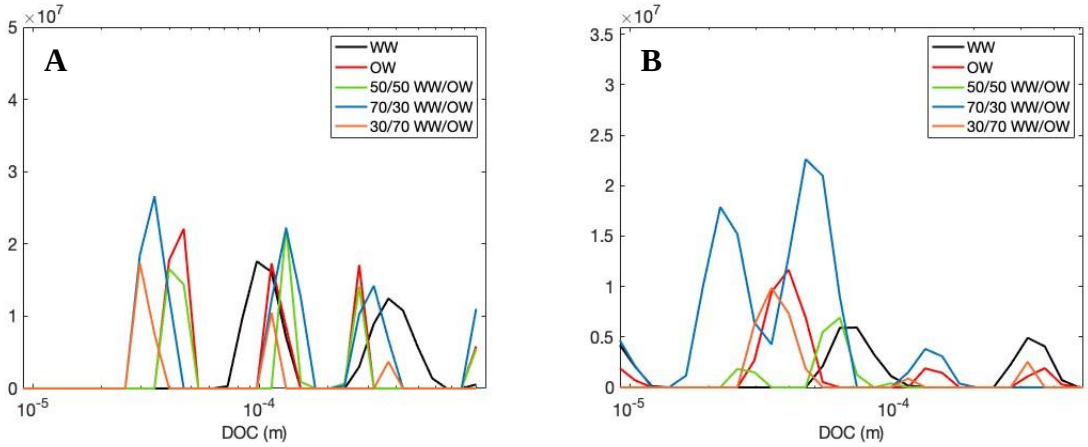

Figure 4.15 DOC distributions at +6mm (A) and -6mm (B) for primary oil drive (5PV) in water.

Figure **4.15** shows the DOC distributions at both +6mm (**A**) and -6mm (**B**) for the primary oil drive at 5PV. The peaks in the DOC distribution for +6mm seems to be very similar, but for -6mm this is not as clear.

4.3.2 Oil signal for the fluid specific DOC distributions

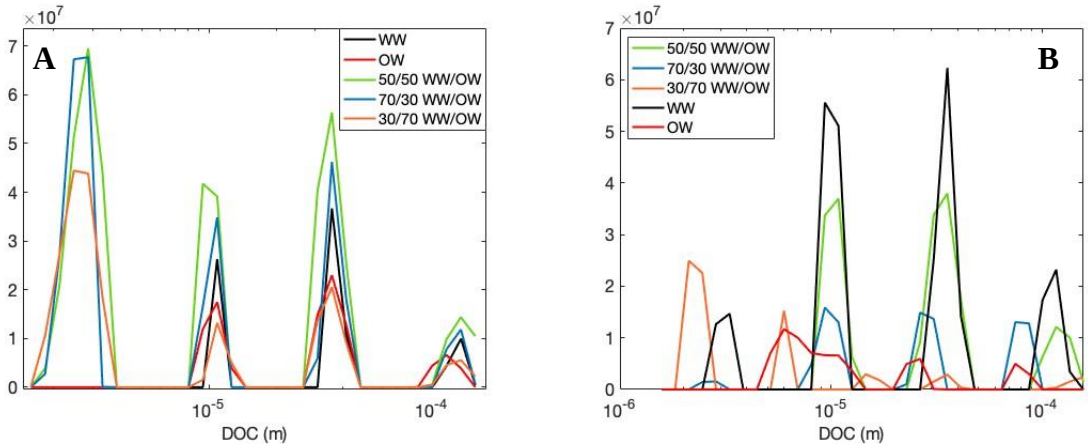

Figure 4.16 DOC distributions at +6mm for primary oil drive (A) and primary water drive (B).

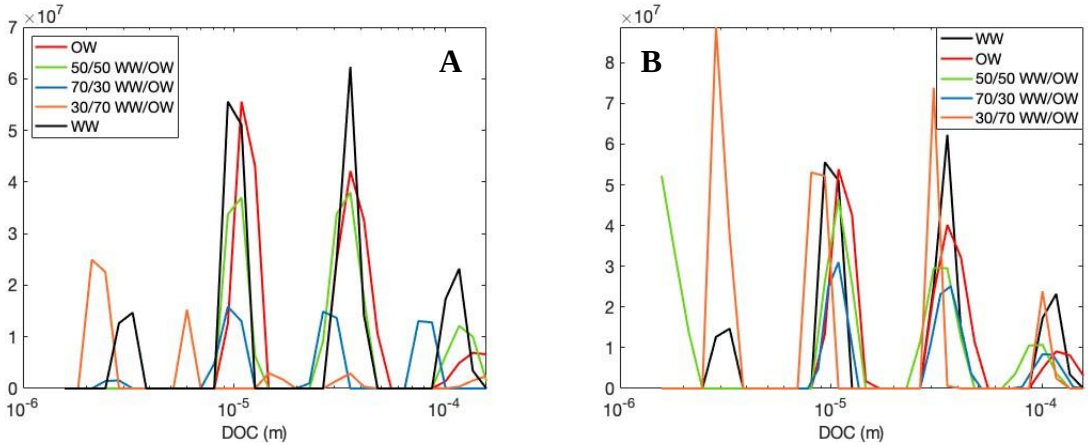

Figure 4.17 DOC distributions at -6mm for primary oil drive (A) and primary water drive (B).

These two figures show the DOC distribution of the oil signal for the primary oil and water drive at +6 and -6mm. The interpretation of these seems to be somewhat more difficult as for the water signal.

5 Discussion

Five different samples, all with two repeated measurements, with varying degree of wettability were investigated. Samples with a mix of water-wet and oil-wet sand has never been analyzed using the advanced MRI-techniques used in this thesis before. The model system that has been developed for this type of testing consist of a very pure quartz sand. This is practically without paramagnetic impurities, which makes it ideal to use in a sample with both oil and water present in the sample. The peaks of oil and water are therefore distinguishable from each other based on their respective chemical shifts.

When processing the data from all the acquisitions it was found to be best to use slices at +6 mm and -6mm from iso center, which sums up to a range of 12 mm. The probe used produces a constant field in the 20 mm range (±10mm). It was also decided to use the data from 0.5PV of both the primary oil drive and the primary water drive. At this stage it would be expected that the top slice (+6mm) is the least affected by the displacement of oil, and the lower slice (-6mm) has been most affected.

For the sample containing 30% water-wet and 70% oil-wet sand it is possible to see from figure **4.5** that the displacement front at 0.5PV primary oil drive was not in the middle of the sample, and therefore data from 1PV was used for this specific sample. This is because the displacement front at 1PV looks to be almost at isocenter.

5.1 Displacement experiments

The oil-wet sample showed viscous fingering, and this is likely due to the oil penetrating through the sample having surface contact. In the water-wet sample the oil does not have surface contact and is expected to move through the pores with a small volume of water along the surface. At residual oil saturation ($S_{o,r}$) the oil retention is much higher in the oil-wet sample as compared to the water-wet. This is evident from the MR-images.

The interpretation of the MR-images for the mixed wettability samples is not as clear. In these samples the oil will have surface contact with parts of the sand, and not with other. During the

preparation of the sample system all samples were prepared with the same protocol, but it is not known how the oil-wet and water-wet sand interacts in this mixing.

5.2 Comparison of repeat measurement

Figure **4.6** – **4.8** shows the water signal and figure **4.9** – **4.11** shows the oil signal, from DOC distributions acquired at 0.5PV of the primary oil drive. All other graphs used for comparing the results of the repeat measurements is in appendix **B**. Comparing the repeat measurement to further validate the method made by Sørgård et. al.[10].

Comparing the repeated measurements of the DOC distributions at 0.5PV primary oil and water drive (figure **4.6**-**4.11**, appendix **B**) shows a

5.3 The dimension of confinement

In the work presented in this thesis five samples were investigated with a fluid specific dimension of confinement (DOC) distributions. DOC distributions are fluid specific and give a length scale for each individual fluid in the sample. In this thesis these fluids were oil and water, which are immiscible. $G_0 - \Delta\chi_{app}$ correlations are used for the calculation of the DOC distributions. $\Delta\chi_{app}$ is calculated from the spectral half with ($\Delta\nu$) because of both oil and water present in the sample during the displacement experiment. Normally T_2^*(from the FID) would be used for the calculation of $\Delta\chi_{app}$ but fluid specific results cannot be obtained from the FID.

DOC distributions displayed in figure **4.12** – **4.17** are similar, which indicates comparable sample geometry.

The axial slices used in this thesis spanned +6mm and -6mm with respect to iso centre of the probe. The probe used produces a constant field in a 20 mm range (±10 mm).

The MR-images from the displacement experiments showed that the oil displacement front did not be uniform inn all the samples. In any case, it will be obvious that there is more oil in the -6mm axial slice at 0.5PV of the primary oil drive, than the +6mm slice. Analyzing the trends of the DOC distributions for the oil signal in figure **4.17A** shows that for the water-wet sample

there is more oil in the biggest pores. This is seen from the difference in intensity between the peaks for the water-wet sample. This is logical as the oil will find the path of least resistance in the sample (large pores). For the oil-wet sample its shown that there is more oil in lower values of DOC. This is also logical as the oil will have surface contact when penetrating through the sample, and therefore be able to access the smaller pores in the sample as well. For the 50/50 water-wet/oil-wet sample it seems like there is a more equal distribution of the DOC, and this also logical if there is the same amount of water-wet and oil-wet sand. The sample containing 70/30 water-wet/oil-wet shows a very equal distribution which means the oil will penetrate small and large pores in this sample. For the 30/70 water-wet/oil-wet sample it seems like there will be more oil in the lower values of DOC. This can be explained with the oil having more surface contact in this sample due to the high degree of oil-wet sand in the system. The missing of the DOC distribution peak in the figures for the water-wet sample is possibly due to high repressing. Surface contact will lead to a low $G_0 - \Delta\chi_{app}$ correlation, and if this is repressed to much no peak will be visible in the figures. This is apparent later on in the figures also.

Looking at the same axial slice but analyzing the water signal of the DOC in figure **4.13A** it shows that the water-wet sample have only one peak on the higher side of the DOC. The rest of the samples shows a trend which is logical for each sample. The 70/30 water-wet/oil-wet sample have a peak at the same DOC value as for water-wet sample, but it also displays a peak at a lower DOC value. This lower DOC value is possibly due to the oil displacing into the sample. This will lead to the oil finding the way of the least resistance and leaving the water almost as a membrane between the oil and the surface. Surface contact will lead to a low $G_0 - \Delta\chi_{app}$ correlation for the water and lead to a lower DOC value. The same explanation can describe and explain the DOC distribution for all the other samples.

The +6mm slice would be expected to have been less affected by the displacing oil in the primary oil drive 0.5PV. Figure **4.16A** shows the oil signal for the primary oil drive 0.5PV at +6mm. Here both the water-wet and oil-wet samples display almost the same trends and behavior of the DOC distribution. Both these samples show a higher value of DOC distribution, and that is logical as the oil that has progressed this far in the sample has done so by the biggest pores. Visually this is also seen in figure **4.1** and **4.2**, as it is seen that the displacement front is at almost 0.5PV. All the samples with mixed wettability seem to show almost the same trend

in this slice. All show a lower DOC value which implies that oil has progressed to smaller pores in these samples.

The water signal for the +6mm slice of the primary oil drive 0.5PV (figure **4.12A**) shows to peaks at the higher DOC values for the water-wet sample. This is logical as it seems from the MR-images (figure **4.1**) that not a lot of oil has progressed this far in this sample. For the water-wet sample it is shown that there is only DOC distribution in the higher values. For the 70/30 water-wet/oil-wet this shows the same as for the water-wet and this is not to be expected. In this sample a lower DOC value would be expected as for all other samples, and in other axial slices. Figure **4.13** was made by removing the water signal from water-wet and 30/70 water-wet/oil-wet samples. In this figure it is shown that the trend is an increase in intensity in the lower DOC values with an increase in oil-wet sand (OW > 50/50 WW/OW > 70/30 WW/OW). This trend is logical as the more oil-wet sand present in the sample the smaller the pores/DOC the water will occupy.

Figure **4.15** shows the DOC distributions for the water signal at +6mm (**A**) and -6mm (**B**) for the primary oil drive 5PV, also known as irreducible water saturation ($S_{w,i}$). At this point the water in the sample is thought to be irreducible. Figure **4.15A** shows that in the +6mm axial slice the values and intensities for all samples are almost the same. This leads to believe that almost the same amount of water is irreducible in all the samples, except the water-wet. This sample shows no lower value DOC, so in this sample the water still possesses a higher DOC value (bigger pores). The -6mm (**B**) figure is not as easy to analyze but shows some of the same trend as for the +6mm axial slice.

The water signal from the primary water drive 0.5PV at +6mm (figure **4.12B**) shows that the two samples with the highest amount of water-wet sand have a water signal in the lower DOC values. When displacing the oil in the sample it is believed that the water will enter along the surface because of the surface contact, and that the oil will in some of the bigger pores will stay put in the middle of the pores. This will lead to a lower DOC value because of the low $G_0 - \Delta\chi_{app}$ correlation because of the surface contact. For the oil-wet, 50/50 water-wet/oil-wet and 30/70 water-wet/oil-wet samples, the trend is that the intensity of the signal increases with the increasing amount of oil-wet sand. The oil signal from the same slice and displacement (figure **4.16B**) is not as easy to interpret. But it seems that the trend is that with increasing oil-wet sand present in the sample the smaller the DOC values become. This is apparent for all samples

except the oil-wet which must be described as an outlier. The lower DOC values with increasing oil-wet wettability are logical as this is the primary water drive. The water will therefore displace the oil using the path of least resistance (bigger pores) with the increasing amount of oil-wet sand and decreasing amount of surface contact for the water.

For the primary water drive 0.5PV for the water signal in the -6mm axial slice (figure **4.14B**) the DOC distribution seems to be almost the same for all samples. The MR-images for the primary water drive (figure **4.1-4.5**) shows that the displacement front in these is not as uniform as for the primary oil drive. If looking at the oil-signal for the primary water drive 0.5PV in the same slice (figure **4.17B**) shows some of the same tendencies as for the water signal. These slices in this displacement will therefore not be a good method do try and differentiate between wettability in a sample.

5.4 Reproducibility with unknown wettability

In the work for this thesis was testing these advanced MRI techniques on samples with different wettability than previous work. The hope is that it will be possible to do a blinded experiment with the same model system, and then compare the results to the data obtained during the experiments in this thesis.

Looking at the data this seems to a feasible experiment. Some of the DOC distributions showed clear trends that would lead to believe that doing a blinded experiment with a mixed wettability would lead to a possibility to determine the wettability of the sample. Figure **4.13** is an example of a trend that it is thought could do this.

5.5 Conclusion

The aim of this thesis was to measure the correlation between the internal gradient and the line width ($G_0 - \Delta\nu$), and map how the limited geometry of the fluids is affected when changing the wettability and pore geometry in a porous media based on the mineral-surface. This aim is believed to have been achieved through thorough experimental work and analyzation in this thesis. It is possible to see the limited geometry on the fluids is affected when changing the wettability.

5.6 Further work

Further research could include testing on blinded/unknown systems as described earlier. Testing of the DOC method could also be done on actual carbonate rocks. This might be challenging as the DOC distributions are calculated from the spectral half widths ($\Delta\nu$) of the oil and water peaks, and it requires a relatively high magnetic field strength to separate them based on chemical shift. Sandstones might not be suitable due to the high paramagnetic impurities, but carbonate rock have much less paramagnetic impurities. This way it would be possible to see if DOC distributions can provide wetting indications in actual carbonate rocks.

Only a fraction of all data collected during the experiments has been presented in this thesis. If interested in accessing the data, contact the author or supervisor John Georg Seland, Department of Chemistry, University of Bergen.

Bibliography

[1] A. B. Zolotukhin and J.-R. Ursin, *Introduction to petroleum reservoir engineering*. Kristiansund: Høyskoleforlaget, 2014.

[2] E. Amott, "Observations Relating to the Wettability of Porous Rock," *Trans. AIME*, vol. 216, no. 01, pp. 156–162, Dec. 1959, doi: 10.2118/1167-G.

[3] E. C. Donaldson Member Aime, R. D. Thomas, and P. B. Lorenz, "Wettability Determination and Its Effect on Recovery Efficiency," *Soc. Pet. Eng. J.*, vol. 9, no. 01, pp. 13–20, Mar. 1969, doi: 10.2118/2338-PA.

[4] F. Bloch, W. W. Hansen, and M. Packard, "Nuclear induction [5]," *Physical Review*, vol. 69, no. 3–4. American Physical Society, p. 127, Feb. 1946. doi: 10.1103/PhysRev.69.127.

[5] E. M. Purcell, H. C. Torrey, and R. V. Pound, "Resonance absorption by nuclear magnetic moments in a solid [7]," *Physical Review*, vol. 69, no. 1–2. American Physical Society, pp. 37–38, Jan. 1946. doi: 10.1103/PhysRev.69.37.

[6] R. J. S. Brown, I. Fatt, and M. Athie, "Measurements Of Fractional Wettability Of Oil Fields' Rocks By The Nuclear Magnetic Relaxation Method," Oct. 1956, doi: 10.2118/743-G.

[7] R. L. Kleinberg and J. A. Jackson, "An introduction to the history of NMR well logging," *Concepts Magn. Reson.*, vol. 13, no. 6, pp. 340–342, 2001, doi: 10.1002/CMR.1018.

[8] J. Mitchell, T. C. Chandrasekera, D. J. Holland, L. F. Gladden, and E. J. Fordham, "Magnetic resonance imaging in laboratory petrophysical core analysis," *Phys. Rep.*, vol. 526, no. 3, pp. 165–225, May 2013, doi: 10.1016/J.PHYSREP.2013.01.003.

[9] A. M. L. Bratland and J. G. Seland, "Multidimensional dynamic NMR correlations in sedimentary rock cores at different liquid saturations," *J. Magn. Reson.*, vol. 327, p. 106963, Jun. 2021, doi: 10.1016/J.JMR.2021.106963.

[10] H. N. Sørgård and J. G. Seland, "A fluid specific dimension of confinement as a measure of wettability in porous media," *J. Magn. Reson.*, vol. 310, pp. 1–10, 2020, doi: 10.1016/j.jmr.2019.106663.

[11] A. M. Løkkevik Bratland, T. Pavlin, K. Djurhuus, and J. G. Seland, "Characterising oil and water in porous media using correlations between internal magnetic gradient and transverse relaxation time," *J. Magn. Reson.*, vol. 310, p. 106649, Jan. 2020, doi:

10.1016/j.jmr.2019.106649.

[12] H. N. Sørgård and J. G. Seland, “Investigating pore geometry in heterogeneous porous samples using spatially resolved G 0 -Δχ app and G 0 -Δν correlations,” *J. Magn. Reson.*, vol. 301, pp. 40–48, Apr. 2019, doi: 10.1016/j.jmr.2019.02.008.

[13] R. T. Lewis and J. G. Seland, “Characterization of pore geometry using correlations between magnetic field and internal gradient,” *Microporous Mesoporous Mater.*, vol. 269, pp. 31–34, Oct. 2018, doi: 10.1016/J.MICROMESO.2017.05.041.

[14] H. Friebolin, *Basic One- and Two-Dimensional NMR Spectroscopy*, 5th ed. Wiley-VCH Verlag GmbH, 2011.

[15] L. G. Hanson, “Is quantum mechanics necessary for understanding magnetic resonance?,” *Concepts Magn. Reson. Part A Bridg. Educ. Res.*, vol. 32, no. 5, pp. 329–340, Sep. 2008, doi: 10.1002/cmr.a.20123.

[16] H. N. Sørgård, “Wetting in Porous Media : A Nuclear Magnetic Resonance Wetting in Porous Media : A Nuclear Magnetic Resonance Study .,” University of Bergen, 2020. [Online]. Available: https://bora.uib.no/bora-xmlui/handle/1956/22665

[17] H. Y. Carr and E. M. Purcell, “Effects of Diffusion on Free Precession in Nuclear Magnetic Resonance Experiments,” *Phys. Rev.*, vol. 94, no. 3, p. 630, May 1954, doi: 10.1103/PhysRev.94.630.

[18] S. Meiboom and D. Gill, “Modified Spin-Echo Method for Measuring Nuclear Relaxation Times,” *Rev. Sci. Instrum.*, vol. 29, no. 8, p. 688, Dec. 2004, doi: 10.1063/1.1716296.

[19] J. Mitchell, T. C. Chandrasekera, M. L. Johns, L. F. Gladden, and E. J. Fordham, “Nuclear magnetic resonance relaxation and diffusion in the presence of internal gradients: the effect of magnetic field strength,” *Phys. Rev. E. Stat. Nonlin. Soft Matter Phys.*, vol. 81, no. 2 Pt 2, Feb. 2010, doi: 10.1103/PHYSREVE.81.026101.

[20] J. Keeler, *Understanding NMR Spectroscopy*. John Wiley & Sons, Ltd, 2010.

[21] M. H. Levitt, *Spin Dynamics: Basics of Nuclear Magnetic Resonance*, 2nd ed. Chichester: John Wiley & Sons, Ltd, 2008.

[22] J. N. Dumez, “Spatial encoding and spatial selection methods in high-resolution NMR spectroscopy,” *Prog. Nucl. Magn. Reson. Spectrosc.*, vol. 109, pp. 101–134, Dec. 2018, doi: 10.1016/J.PNMRS.2018.08.001.

[23] B. Sun and K. J. Dunn, “Probing the internal field gradients of porous media,” *Phys. Rev. E. Stat. Nonlin. Soft Matter Phys.*, vol. 65, no. 5 Pt 1, p. 7, 2002, doi: 10.1103/PHYSREVE.65.051309.

[24] M. D. Hürlimann, K. G. Helmer, T. M. Deswiet, P. N. Sen, and C. H. Sotak, “Spin Echoes in a Constant Gradient and in the Presence of Simple Restriction,” *J. Magn. Reson. Ser. A*, vol. 113, no. 2, pp. 260–264, 1995, doi: 10.1006/JMRA.1995.1091.

[25] M. D. Hürlimann, “Effective Gradients in Porous Media Due to Susceptibility Differences,” *J. Magn. Reson.*, vol. 131, no. 2, pp. 232–240, Apr. 1998, doi: 10.1006/JMRE.1998.1364.

[26] J. Mitchell, T. C. Chandrasekera, M. L. Johns, L. F. Gladden, and E. J. Fordham, “Nuclear magnetic resonance relaxation and diffusion in the presence of internal gradients: the effect of magnetic field strength,” *Phys. Rev. E. Stat. Nonlin. Soft Matter Phys.*, vol. 81, no. 2 Pt 2, Feb. 2010, doi: 10.1103/PHYSREVE.81.026101.

[27] J. Mitchell, T. C. Chandrasekera, and L. F. Gladden, “Obtaining true transverse relaxation time distributions in high-field NMR measurements of saturated porous media: Removing the influence of internal gradients,” *J. Chem. Phys.*, vol. 132, no. 24, p. 244705, Jun. 2010, doi: 10.1063/1.3446805.

[28] P. T. Callaghan, *Provided with courtsey of Paul Callaghan*. 2002.

[29] P. G. Saffman and G. I. Taylor, “The penetration of a fluid into a porous medium or Hele-Shaw cell containing a more viscous liquid,” *Proc. R. Soc. London. Ser. A. Math. Phys. Sci.*, vol. 245, no. 1242, pp. 312–329, Jun. 1958, doi: 10.1098/RSPA.1958.0085.

[30] H. E. L. Rose and M. M. Britton, “Magnetic resonance imaging of reaction-driven viscous fingering in a packed bed,” *Microporous Mesoporous Mater.*, vol. 178, pp. 64–68, Sep. 2013, doi: 10.1016/J.MICROMESO.2013.02.039.

Appendix A– MATLAB scripts

In this appendix, various MATLAB scripts used for data processing in this thesis is presented

A.1 - Butterflies_Oil_water_G0

```
load vdlist;

t=vdlist;

cd('pdata/1');



fid=fopen('2rr','r','n');

data1=fread(fid,'int32');

td1=32;

td2=size(data1);

td2=td2(1)/td1;



ser=data1(1:td2)

% si=2048;

dw=5e-6;

o='pdata';

% p=1;



figure(100); plot(ser); %To inspect the spectrum



f1 = input('Enter the value for left edge of final spectrum ');

% f2 = input('Enter the value for right edge of final spectrum ');
```

```
f2=f1+96

nsec= 2 %input('Number of slices')

m=96/nsec


f=(1:td2)./(2*dw*td2);

[y,i]=max(ser)


f=f-i./(2*dw*td2)

f=f(f1:f2-1);

f_trunk=f(1:m:96);

% f_trunk2=f_trunk+236


ser=ser(f1:f2-1);

figure(101); plot(f,ser);


f3=f2-f1;

save -ascii -tabs f.txt f

save -ascii -tabs f_trunk.txt f_trunk

% save -ascii -tabs f_trunk2.txt f_trunk2

%loop for correction of each ser

td3=td2;

k=1;

td8=f2-f1;
```

```
for i=1:td1
    spec1(:,i)=data1(k:td3);
    I=data1(k:td3);

    I1(i)=mean(I);
    td6=nsec %Number of slices
    td4=(td8/td6);
    td5=td4;
    I=f1;
    td4=I+td4
    for j=1:td6
        I5(i,j)=mean(I(I:td4));
        I=I+td5;
        td4=td5+td4;
    end

    k=k+td2;
    td3=td3+td2;
end
cd ../../
It=strcat('I5','.txt');
save(It,'I5','-ascii','-tabs');

te = 50;
```

```
te=te/1000;


filename_G0=strcat('vclist');

l12=load(filename_G0);

n=size(l12,1);

gam= 26751;


gam2=(gam^2);

t_G0=(1/3)*gam2*te*(0.5*te./l12).^2;

cd('pdata/1');


filename_tG0_o=strcat('t_G0_o.txt');

save(filename_tG0_o, 't_G0', '-ascii', '-tabs');


filename_tG0_w=strcat('t_G0_w.txt');

save(filename_tG0_w, 't_G0', '-ascii', '-tabs');


figure

toILT=l5(1,:);

plot(f_trunk,toILT)


figure

decay_water=l5(:,1);

save -ascii -tabs decay_water.txt decay_water
```

```
plot(t_G0, decay_water)


figure

decay_oil=I5(:,2);

save -ascii -tabs decay_oil.txt decay_oil

plot(t_G0,decay_oil)

cd ../../
```

A.2 - plot_G0_simple_water

```
filename_t_G0=strcat('t_G0_w.txt.out');

t_G0_out=load(filename_t_G0);


filename_I_G0=strcat('decay_water.txt.out');

I_G0_out=load(filename_I_G0);

I_G0 = I_G0_out


D=2.3e-5

G0_verdier=1./t_G0_out;

G0_verdier=sqrt(G0_verdier./D);


figure(201); plot(G0_verdier, I_G0, 'k-')

set(gca,'xscale','log')

xlabel('log(G0)');

set(gca,'fontsize',16)
```

```
set(findall(gca,'Type','Text'),'FontSize',16)

saveas(201,'G0_w.fig')

saveas(201,'GO_w.jpg')


lw = 800

gam= 26751;

DOC = (0.01*2*pi*lw)./(G0_verdier*gam);


figure(202); plot(DOC, I_G0, 'k-')

set(gca,'xscale','log')

xlabel('DOC (m)');

set(gca,'fontsize',16)

set(findall(gca,'Type','Text'),'FontSize',16)

saveas(202,'DOC_w.fig')

saveas(202,'DOC_w.jpg')
```

A.3 - plot_G0_simple_oil

```
filename_t_G0=strcat('t_G0_o.txt.out');

t_G0_out=load(filename_t_G0);


filename_I_G0=strcat('decay_oil.txt.out');

I_G0_out=load(filename_I_G0);

I_G0 = I_G0_out
```

```
D=4.5e-7

G0_verdier=1./t_G0_out;

G0_verdier=sqrt(G0_verdier./D);


figure(203); plot(G0_verdier, I_G0, 'k-')

set(gca,'xscale','log')

xlabel('log(G0)');

set(gca,'fontsize',16)

set(findall(gca,'Type','Text'),'FontSize',16)

saveas(203,'G0_o.fig')

saveas(203,'GO_o.jpg')


lw = 1000

gam= 26751;

DOC = (0.01*2*pi*lw)./(G0_verdier*gam);


figure(204); plot(DOC, I_G0, 'k-')

set(gca,'xscale','log')

xlabel('DOC (m)');

set(gca,'fontsize',16)

set(findall(gca,'Type','Text'),'FontSize',16)

saveas(204,'DOC_o.fig')

saveas(204,'DOC_o.jpg')
```

Appendix B – Comparison of repeat measurements

B.1 Water signal for fluid specific DOC distribution

B.1.1 Water signal for water-wet samples.

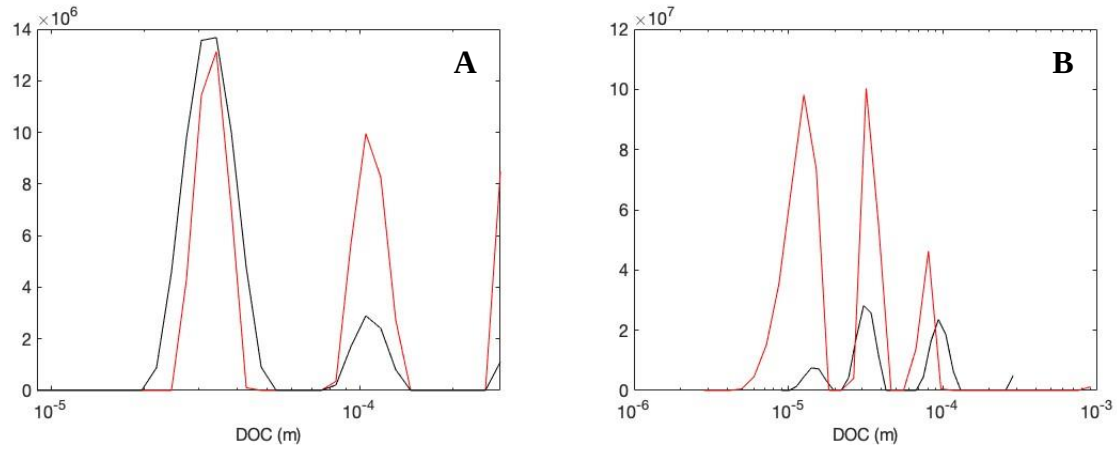

Figure B.1 DOC distributions at +6mm for primary oil drive (A) and primary water drive (B).

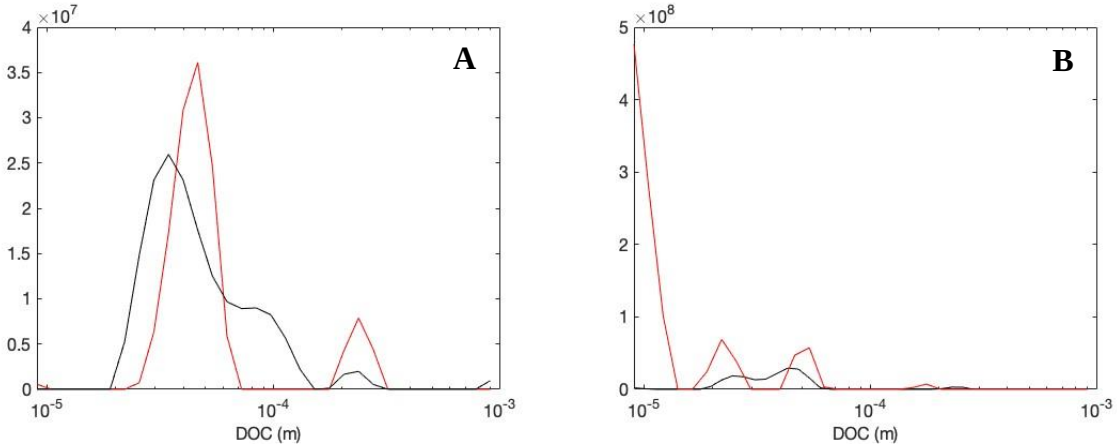

Figure B.2 DOC distributions at -6mm for primary oil drive (A) and primary water drive (B).

B.1.2 Water signal for oil-wet samples.

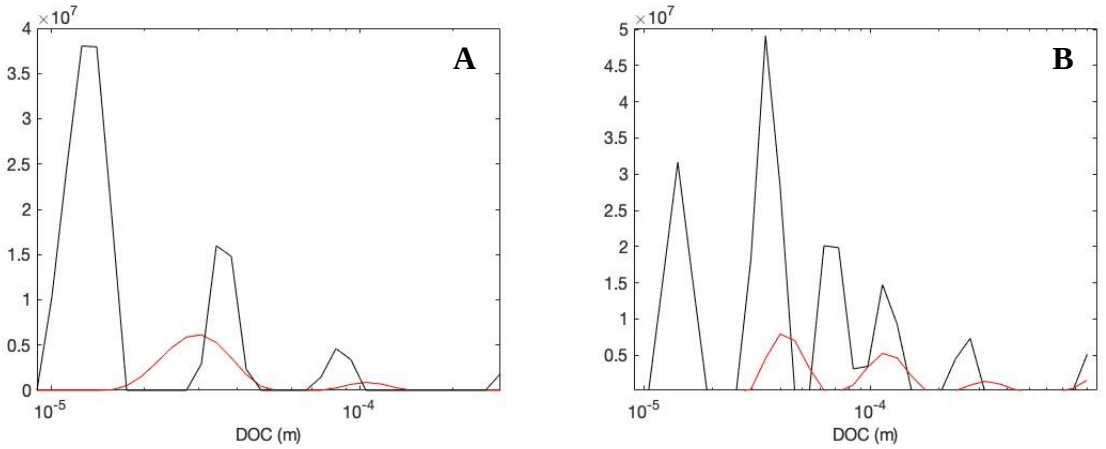

Figure B.3 DOC distributions at +6mm for primary oil drive (A) and primary water drive (B).

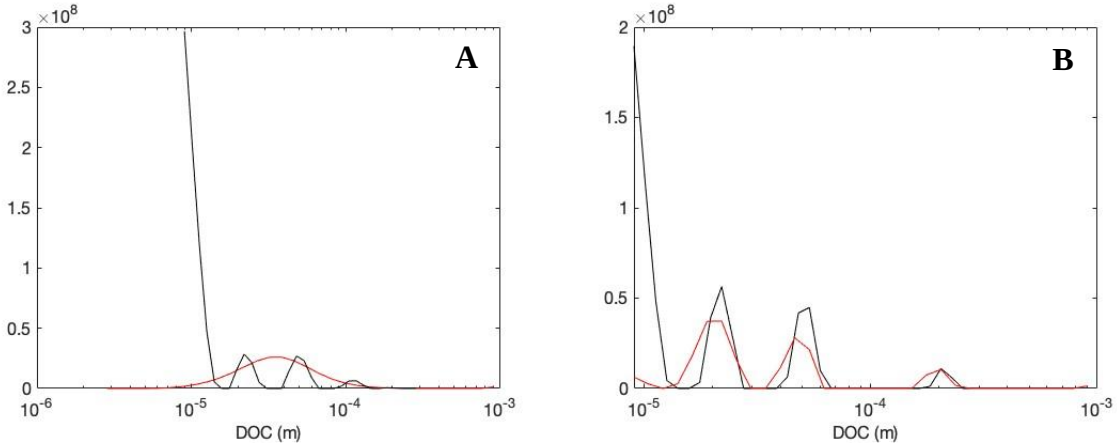

Figure B.4 DOC distributions at -6mm for primary oil drive (A) and primary water drive (B).

B.1.3 Water signal for samples containing 50% water-wet and 50% oil-wet sand.

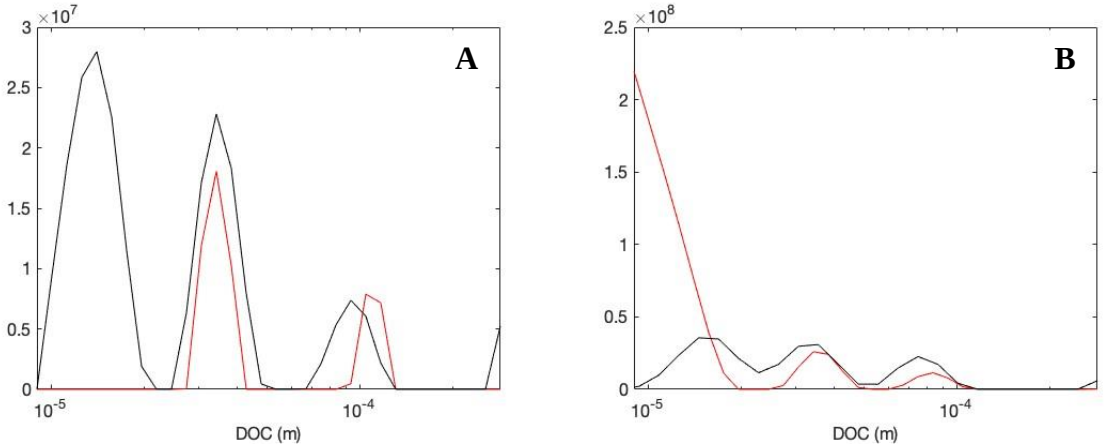

Figure B.5 DOC distributions at +6mm for primary oil drive (A) and primary water drive (B).

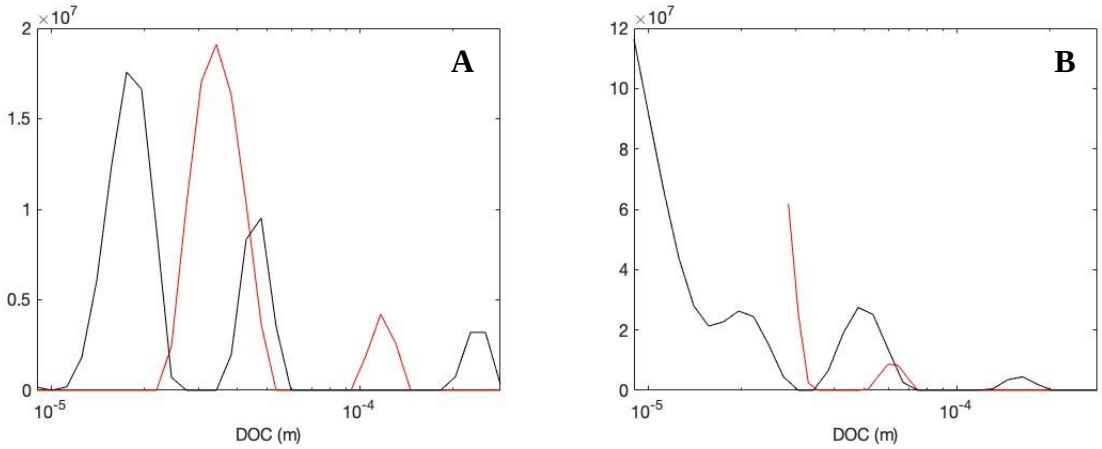

Figure B.6 DOC distributions at -6mm for primary oil drive (A) and primary water drive (B).

B.1.4 Water signal for samples containing 70% water-wet and 30% oil-wet sand.

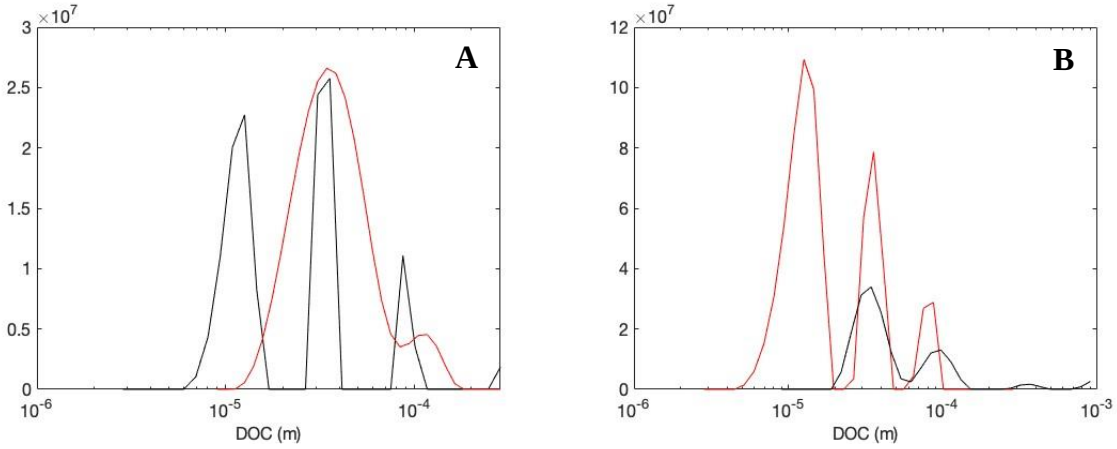

Figure B.7 DOC distributions at +6mm for primary oil drive (A) and primary water drive (B).

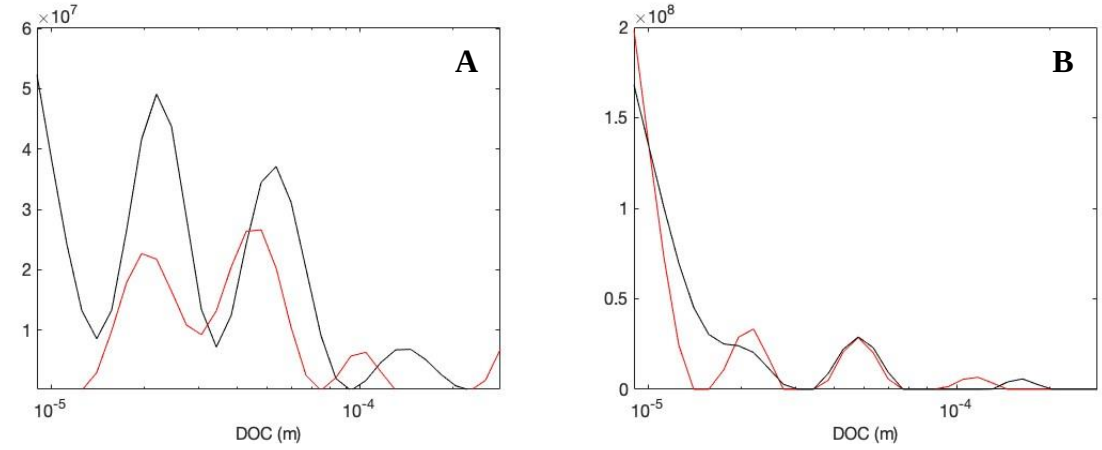

Figure B.8 DOC distributions at -6mm for primary oil drive (A) and primary water drive (B).

B.1.5 Water signal for samples containing 30% water-wet and 70% oil-wet sand.

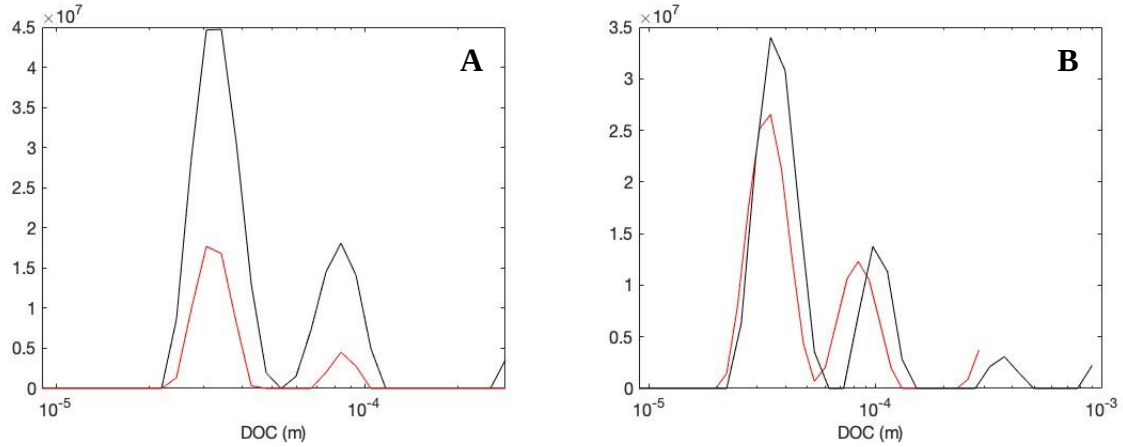

Figure B.9 DOC distributions at +6mm for primary oil drive (A) and primary water drive (B).

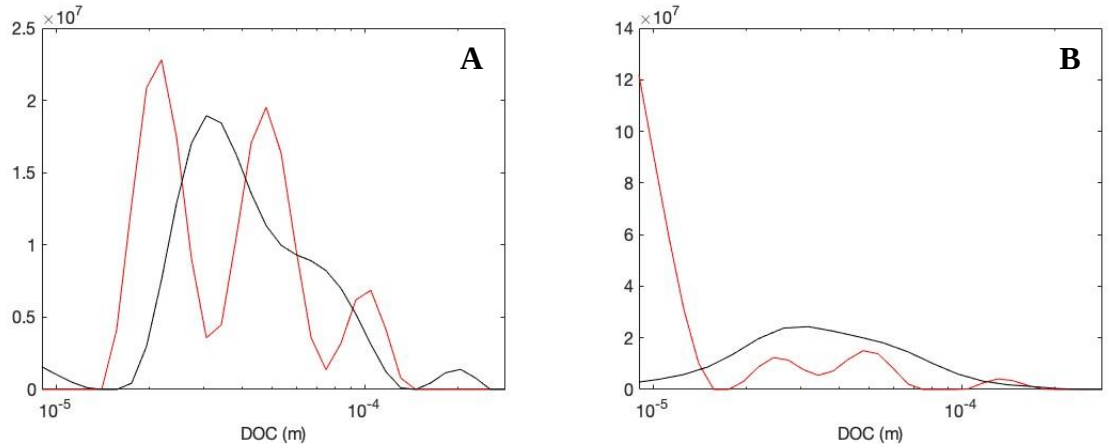

Figure B.10 DOC distributions at -6mm for primary oil drive (A) and primary water drive (B).

B.2 Water signal for fluid specific DOC distribution

B.2.1 Oil signal for water-wet samples.

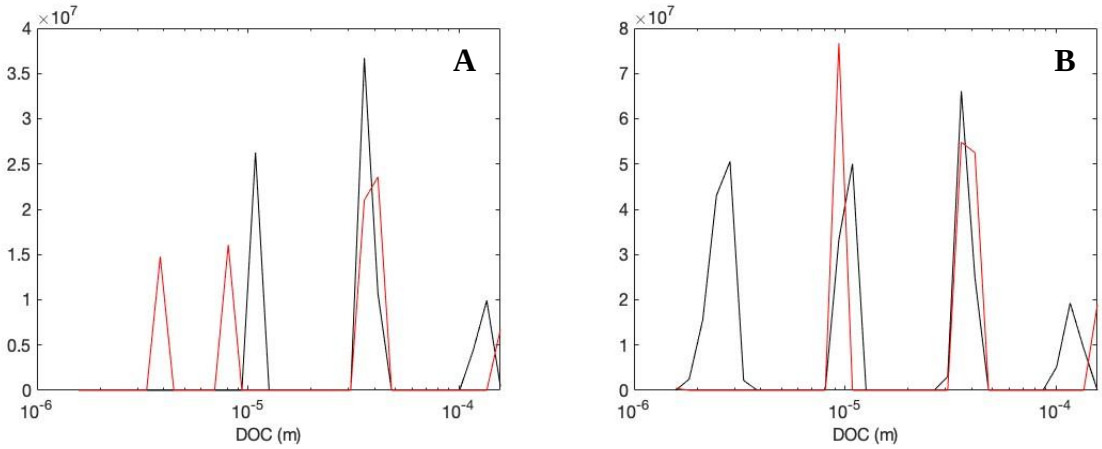

Figure B.11 DOC distributions at +6mm for primary oil drive (A) and primary water drive (B).

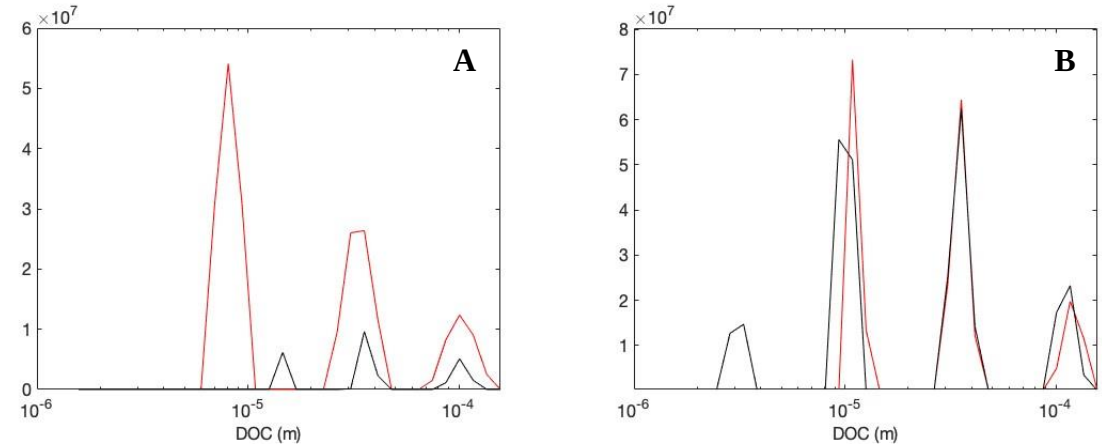

Figure B.12 DOC distributions at -6mm for primary oil drive (A) and primary water drive (B).

B.2.2 Oil signal for oil-wet samples.

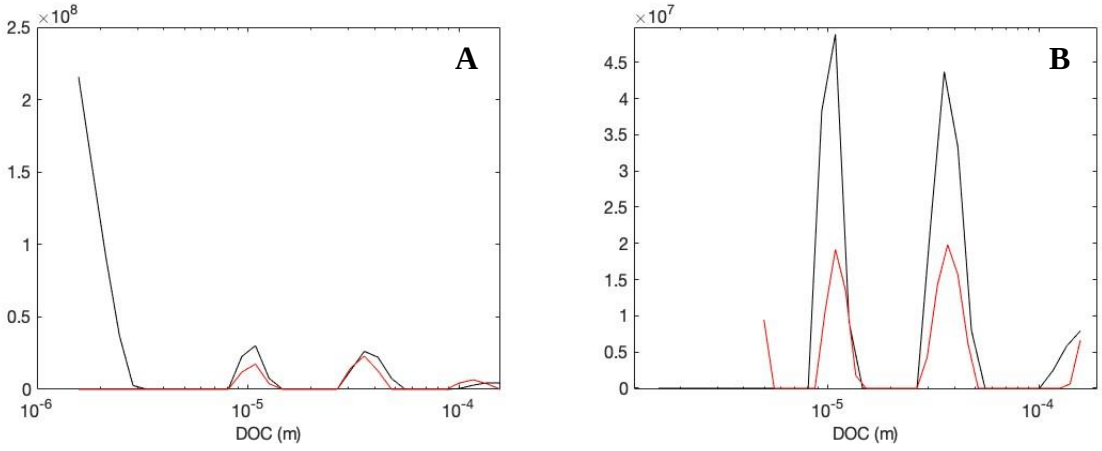

Figure B.13 DOC distributions at +6mm for primary oil drive (A) and primary water drive (B).

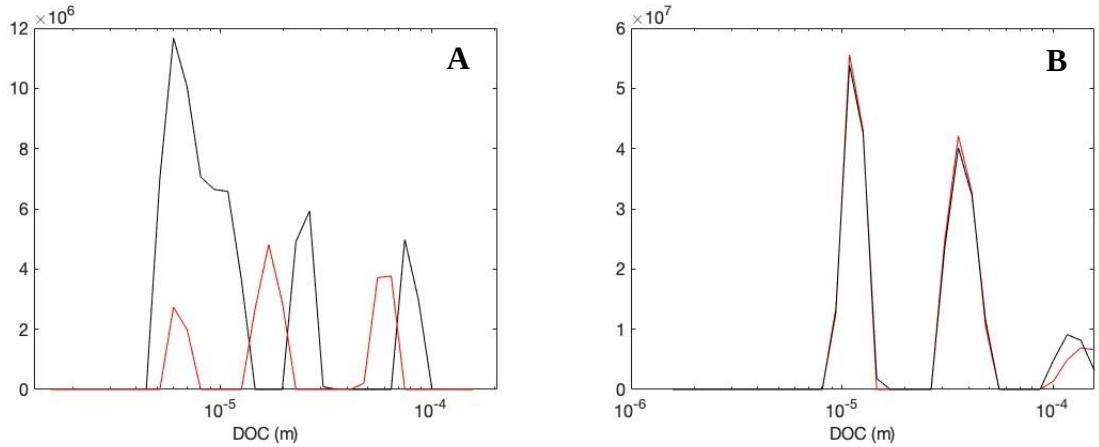

Figure B.14 DOC distributions at -6mm for primary oil drive (A) and primary water drive (B).

B.2.3 Oil signal for samples containing 50% water-wet and 50% oil-wet sand.

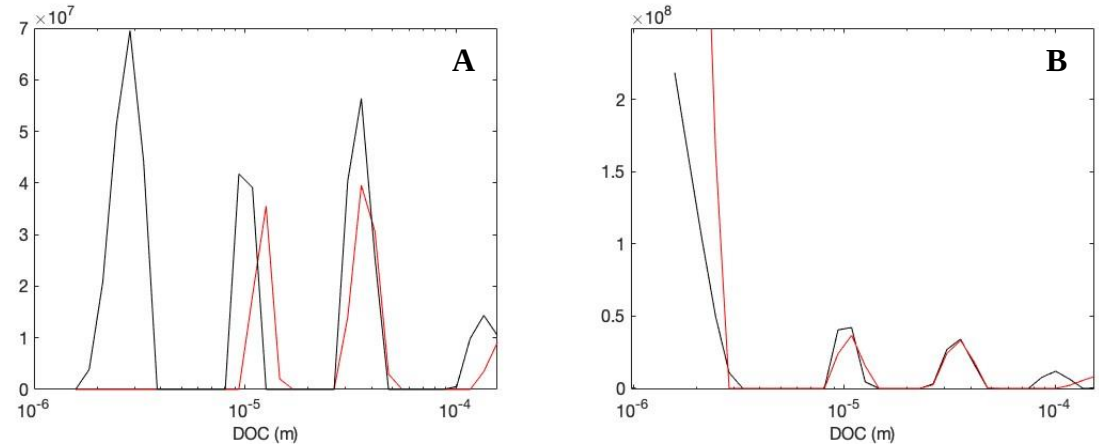

Figure B.15 DOC distributions at +6mm for primary oil drive (A) and primary water drive (B).

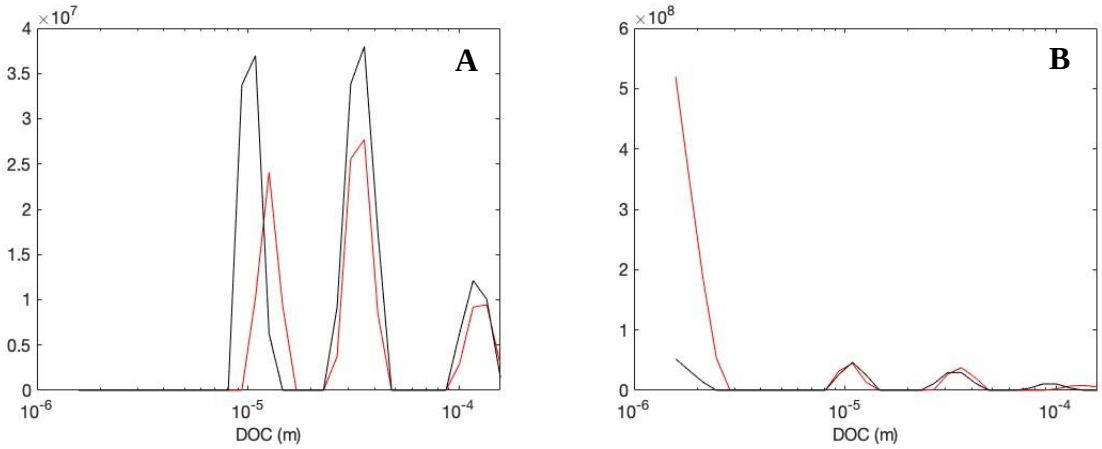

Figure B.16 DOC distributions at -6mm for primary oil drive (A) and primary water drive (B).

B.2.4 Oil signal for samples containing 70% water-wet and 30% oil-wet sand.

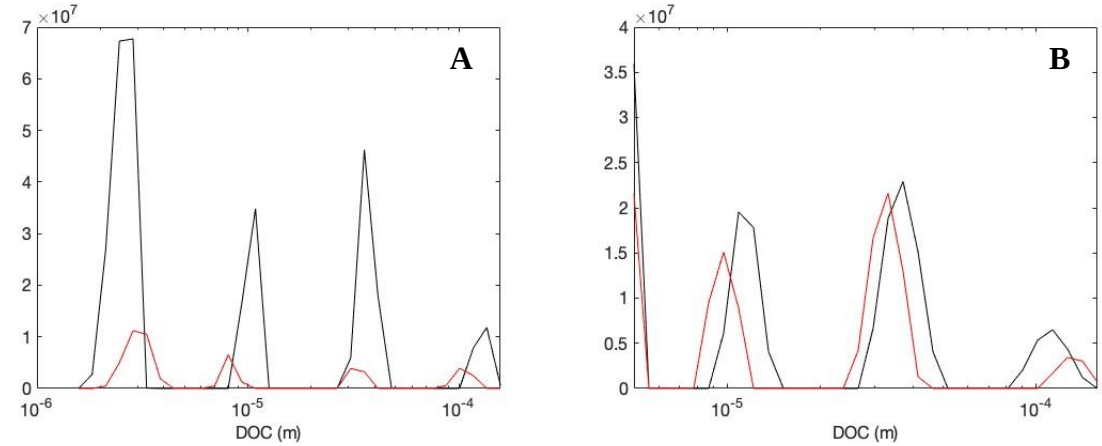

Figure B.17 DOC distributions at +6mm for primary oil drive (A) and primary water drive (B).

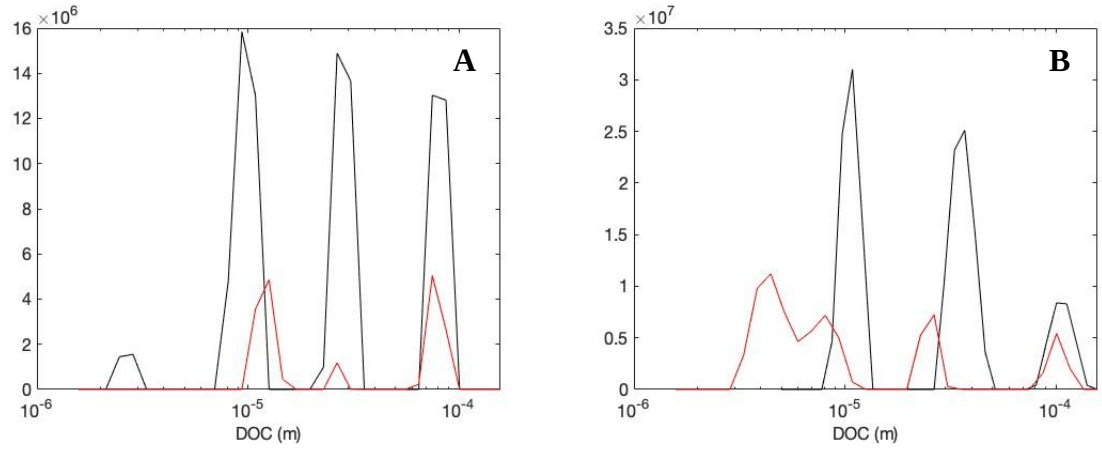

Figure B.18 DOC distributions at -6mm for primary oil drive (A) and primary water drive (B).

B.2.5 Oil signal for samples containing 30% water-wet and 70% oil-wet sand.

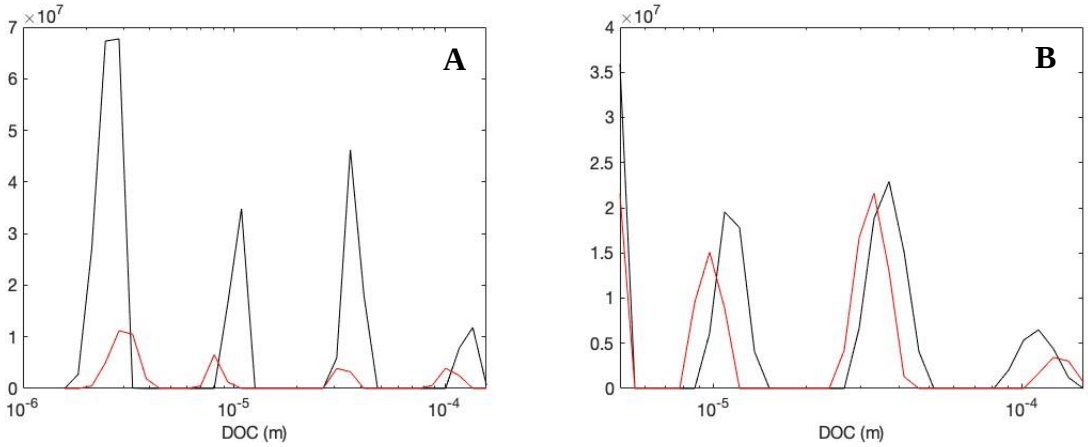

Figure B.19 DOC distributions at +6mm for primary oil drive (A) and primary water drive (B).

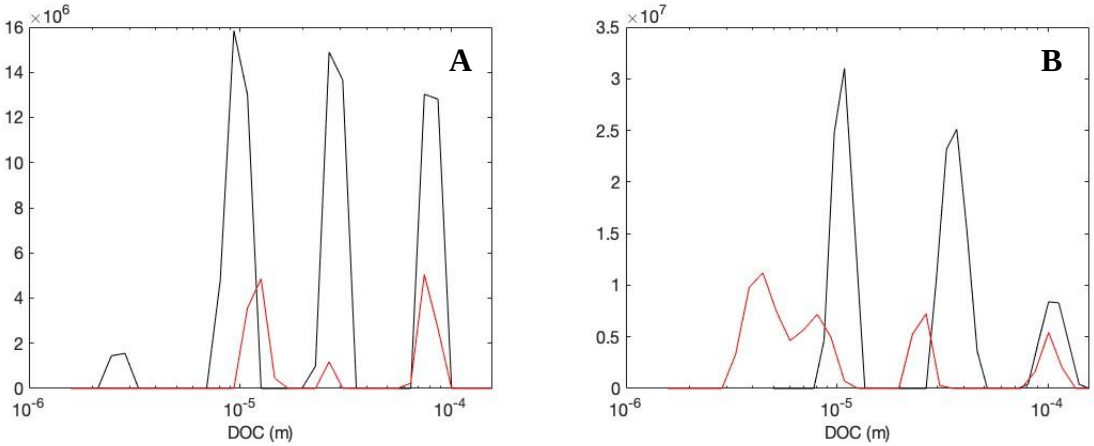

Figure B.20 DOC distributions at -6mm for primary oil drive (A) and primary water drive (B).